Emergent Materials
https://doi.org/10.1007/s42247-024-00793-z

ORIGINAL ARTICLE

How the incorporation synthesis method of the active phase affects the catalytic behavior: Ni/ceo$_2$ nanowires towards ethanol steam reforming

Felipe A. e Silva[1] · André M. Batista[2] · Henrique P. Pacheco[3] · Vera M. M. Salim[3] · Thenner S. Rodrigues[1]

Received: 17 May 2024 / Accepted: 9 July 2024
© Qatar University and Springer Nature Switzerland AG 2024

Abstract
The controlled synthesis of well-defined nanoparticles is crucial for producing optimized catalysts with enhanced properties and maximizing the desired product in catalysis. Therefore, the incorporation of Ni onto CeO_2 nanowires via four different routes was utilized to investigate the effect of metal-support interaction, particle size, and distribution of Ni over the CeO_2 nanowires. This aimed to correlate the physicochemical properties of the obtained Ni/CeO_2 nanowires with their high performance in the steam reforming of ethanol. Specifically, Ni/CeO_2 nanowires were obtained through: (i) incipient wet impregnation, (ii) nanoparticle impregnation, (iii) urea-assisted deposition, and (iv) $NaBH_4$-assisted deposition. These methods resulted in four nanostructures with distinct Ni particle sizes and distributions on the surface of CeO_2 nanowires, leading to differences in textural properties, the concentration of oxygen vacancies, and the degree of Ni-CeO_2 interaction. The best catalyst, obtained via incipient wet impregnation, exhibited high selectivity to H_2 (65%, considering that the maximum theoretical selectivity is 66%) in the catalytic tests, along with 100% ethanol conversion and minimal deactivation (6% within 24 h and 20% within 48 h) during the catalytic test. Thus, it was observed that controlled synthesis enabled the production of four different nanomaterials with enhanced properties, such as textural properties and concentration of oxygen vacancies, resulting in upgraded catalytic performance.

Keywords Nanoparticle engineering · Catalyst development · Synthesis strategies · Nanowire morphology · Catalytic reactivity

1 Introduction

Nanomaterials have revolutionized the material science field due to their enhanced properties compared to bulk materials, exhibiting improved quantum effects, bioactivity, and surface properties, such as catalytic activity [1]. Particularly, the surface properties of the nanomaterials emerge from the reduction of particle size, leading to direct changes in electronic and structural properties, including lattice parameters, the surface-to-volume ratio, and surface energy of the nanomaterial [2, 3]. Moreover, the surface energy important to determine the intensity of the chemical bond between the nanomaterial and a molecule or an intermediate during a chemical reaction, such as in heterogeneously catalyzed systems [4, 5]. Supported heterogeneous catalysts have been developed to minimize cost and particle size, and maximize dispersion of the active phase and catalytic activity [6–10]. However, the synthesis methods of these catalysts still face limitations in controlling the textural and physicochemical properties, primarily due to irregular surface structures that display varying surface energy on each exposed crystalline plane [4, 11].

The controlled synthesis of nanomaterials can optimize their properties, allowing for precise control over each

✉ Thenner S. Rodrigues
thenner@pent.coppe.ufrj.br

1 Nanotechnology Engineering Program, Alberto Luiz Coimbra Institute for Graduate Studies and Research in Engineering, Federal University of Rio de Janeiro, Av. Horácio Macedo, 2030, 21941-972 Rio de Janeiro, RJ, Brazil

2 Nanosciences and Advanced Materials Program, Federal University of ABC, Av. dos Estados, 5001, 09210-580 Santo André, SP, Brazil

3 Chemical Engineering Program, Alberto Luiz Coimbra Institute for Graduate Studies and Research in Engineering, Federal University of Rio de Janeiro, Av. Horácio Macedo, 2030, 21941-972 Rio de Janeiro, RJ, Brazil

Published online: 20 July 2024

component of supported catalysts, including support and active phase. Various methodologies have been employed to synthesize solid supports, such as precipitation [12], sonochemical [13, 14], and sol-gel [15]. Among the methods, the hydrothermal method stands out as a promisor methodology due to its low cost and ability to generate different morphologies with well-defined size, shape, and structure [16–20]. For instance, a study conducted by Soykal et al. investigated the impact of support particle size on the ethanol steam reforming reaction [21, 22]. They observed that CeO_2 microparticles ranging from 20 nm to 0.2 µm, and CeO_2 nanoparticles of 5–8 nm, demonstrated variances in ethanol conversion and H_2 yield. Specifically, CeO_2 nanoparticles exhibited superior ethanol conversion and H_2 yield compared to microparticles [21–23].

The reduction of particle size from macro and microscale, referred to as bulk materials, to nanoscale significantly impacts the properties of the nanoparticles, leading to substantial alterations in their optical, magnetic, electronic, and surface properties [10, 24–26]. In macro form, bulk materials exhibit a limited incorporation of surface atoms within the total atom count, resulting in a lower specific surface area and fewer exposed atoms. In contrast, at the nanoscale, the smaller particle size results in an enhanced specific surface area and a higher number of exposed atoms, promoting distortions in geometric and electronic factors and leading to enhanced properties [27–29].

Additionally, Vecchietti et al. emphasized that the shape of nanostructures significantly influences the catalytic behavior of nanomaterials [30]. They observed that CeO_2 nanooctahedra and nanocubes predominantly expose (111) and (100) surfaces, respectively. Nanocubes were found to produce 2.4 times more hydrogen compared to nanooctahedra, attributed to differences in adsorbed ethoxy species. On CeO_2(111) surfaces, Vecchietti et al. identified monodentate type I and type II ethoxy species, with alkyl chains oriented perpendicular or parallel to the surface. Conversely, CeO_2(100) surfaces exhibited bidentate and monodentate type III ethoxy species, distributed on the O-terminated checkerboard surface and on the pyramid of the reconstructed (100) surface, respectively. The more reactive surface ethoxy species, such as monodentate type I or III on CeO_2 nanooctahedra and CeO_2 nanocubes, respectively, reacted to form acetate species that decomposed into CO_2 and CH_4, with H_2 generated via the recombination of hydroxyl species. Furthermore, the more stable monodentate type II and bidentate ethoxy species on CeO_2 nanooctahedra and nanocubes, respectively, formed an ethylenedioxy intermediate. The binding of this intermediate was facet-dependent: on the (111) facet, the less strongly bound ethylenedioxy desorbed as ethylene, while on the (100) facet, the more strongly bound intermediate also produced CO_2 and H_2 via formate species. In our research, we utilized the hydrothermal method to synthesize CeO_2 nanowires with a narrow size distribution (11 nm ± 2 nm in width) and enhanced surface properties, including oxygen vacancies [18, 19, 31].

Nevertheless, the active phase can be synthesized through two routes: homogeneous or heterogeneous nucleation. In homogeneous nucleation, crystals form uniformly throughout the parent phase in the bulk of the reaction medium, while heterogeneous nucleation occurs in the presence of a second phase (support surface) [32–35]. Homogeneous nucleation typically requires higher energy than heterogeneous nucleation for crystal nucleation [3, 32–35]. In controlled synthesis, the active phase can be synthesized through homogeneous nucleation and subsequently incorporated by adsorption onto the solid support, a process known as impregnation [36]. This method allows for the synthesis of diverse morphologies, such as urchin [37, 38], flowers [39, 40], and hollow nanoparticles [10, 41–43], as well as different sizes [44–46], ranging from larger nanoparticles to thin layers [18]. In contrast, heterogeneous nucleation involves the active phase nucleating over the solid support, offering the ability to achieve different metal-support interactions and particle sizes. However, spherical morphologies are typically obtained [46–48]. Additionally, various methodologies can be employed to synthesize the active phase, including chemical reduction [49], precipitation [50], electrochemical reduction [51], and photo-reduction [52]. Chemical reduction emerges as a prominent method for synthesizing metallic active phases, facilitating the direct formation of metal nanoparticles from metal ions without additional steps. Nickel (Ni) is especially favored as a metallic active phase due to its affordability and distinctive properties, including high surface energy and catalytic activity [53–58].

Furthermore, the size of metallic active phase particles and the interaction between the metal and support are significant factors in conducting a well-controlled catalytic reaction, achieving high hydrogen yield while preventing carbon deposition on the catalyst. Da Silva et al. reported on the effect of metallic particle size using cobalt supported on carbon nanofibers in ethanol steam reforming [59]. To isolate the metallic active phase, they utilized carbon nanofibers that do not exhibit relevant ethanol conversion (~5%). By manipulating the cobalt loading, they were able to control the particle size. Increasing the cobalt loading led to an increase in particle size, ranging from 1.0 to 22 wt% and 2.4 to 16 nm, respectively. As the particle size decreases, the turnover frequency increases due to the higher number of surface atoms, which are more active than those in larger particles [31]. The catalyst containing larger cobalt particles, larger than 4 nm, exhibited a significant decrease in ethanol conversion. Moreover, cobalt particles with the highest size (16 nm) displayed significant deactivation and amorphous

carbon deposition on the catalyst surface after 3 h of reaction [31, 59].

The nanoscale introduces various modifications in geometric and electronic characteristics due to the increased percentage of exposed surface atoms and higher free surface energy, leading to enhanced properties. These modifications promote surface defects, such as kinks, steps, and vacancies, which are more active catalytic sites. For instance, smaller spherical nanoparticles with diameters of 2, 6, and 10 nm can have between 200 and 400, 7,000–10,000, and 34,000–47,000 atoms, respectively [60], corresponding to 50% t 10% o exposed surface atoms [61]. These characteristics can result in higher interaction with the support and more active catalytic sites [62].

The metal-support interaction (MSI) plays a crucial role in heterogeneous catalysts that facilitate reforming reactions for producing renewable hydrogen. This interaction involves modifying the geometric and electronic structure of metal species when they come into contact with supports [31, 63, 64]. Tailoring supports with specific features has been successful in stabilizing metal species, adjusting their geometric and electronic configurations, and improving mass transfer efficiency. Importantly, placing active metal species close to support defects significantly enhances the activation of reactant adsorption, optimizes the transition state of adsorbates, and facilitates the conversion of reaction intermediates [31, 64, 65]. Wang et al. demonstrated these effects by depositing nickel nanoparticles of varying sizes to manipulate the quantity of oxygen vacancies and the metal-support interaction [31]. As the size of nickel particles decreases, there is an increase in nickel dispersion and the number of oxygen vacancies, resulting in enhanced metal-support interaction and higher hydrogen yield [31, 64, 66].

We reported the impact of nanostructures on catalytic activity by employing Ni/CeO_2-Sm_2O_3 nanowires and their bulk analog. The Ni/CeO_2-Sm_2O_3 nanowires exhibited remarkable stability, with 192 h of continuous activity, 60% hydrogen selectivity, and 100% ethanol conversion in ethanol steam reforming [18]. Subsequently, we explored the influence of the nature of the solid support on the catalytic performance of Rh/Mn_xO_y (M = Ce, Ti, Si, Zn, and Al) in ethanol steam reforming [67]. In this paper, we systematically investigate the impact of different incorporation methods of the active phase on the catalytic behavior of Ni/CeO_2 nanowires in ethanol steam reforming, serving as model reaction. The CeO_2 nanowires were synthesized via the hydrothermal method, and we evaluated four different synthetic approaches for incorporating Ni onto the surfaces of the CeO_2 nanowires: (i) wet impregnation of Ni precursor, (ii) wet impregnation of preformed Ni nanoparticles, (iii) deposition assisted by urea, and (iv) deposition assisted by sodium borohydride. Subsequently, we analyzed the physical and chemical properties of the catalysts using various characterization techniques. Finally, we applied the Ni/CeO_2 nanowires catalysts in ethanol steam reforming as a model reaction to produce hydrogen (H_2). Specifically, we aimed to investigate how different incorporation methods of the active phase would impact the catalytic performance of the Ni/CeO_2 nanowires catalysts in terms of activity, selectivity, and stability. Our findings reveal that the incorporation methods of the active phase significantly influence the physicochemical properties of the catalysts, including nanoparticle size, metal dispersion, metal-support interaction. Moreover, the catalytic behavior in ethanol steam reforming, encompassing activity, selectivity, stability, and carbon deposition, is strongly influenced by each employed incorporation methodology.

2 Experimental

2.1 Materials

Analytical grade cerium (III) nitrate hexahydrate ($Ce(NO_3)_3{\cdot}6H_2O$, 99.5%, Sigma-Aldrich), ethanol (C_2H_6O, 99.5%, Sigma-Aldrich), ethylene glycol ($HOCH_2CH_2OH$, 99.8%, Sigma-Aldrich), nickel (II) nitrate hexahydrate ($Ni(NO_3)_2{\cdot}6H_2O$, 99.5%, Sigma-Aldrich), Polyvinylpyrrolidone ($(C_6H_9NO)_n$, 55,000 $g.mol^{-1}$, Sigma-Aldrich), Sodium borohydride ($NaBH_4$, 98.0%, Sigma-Aldrich), sodium hydroxide (NaOH, 99%, Sigma-Aldrich), urea (CH_4N_2O, 99.75%, Vetec), hydrochloric acid (HCl, 37%, Vetec), and nitric acid (HNO_3, 70%, Vetec), were used as received. All glassware were cleaned with aqua regia (HCl: HNO_3 = 3:1) before the synthesis to prevent contamination.

2.2 Synthesis of CeO_2 nanowires

The CeO_2 nanowires were synthesized using the hydrothermal method [19]. In this process, 19.6 g of NaOH were dissolved in 35.0 mL of Milli-Q water in a Teflon bottle under magnetic stirring. Subsequently, 15 mL of an aqueous $Ce(NO_3)_3{\cdot}6H_2O$ solution at 1.4 M was added dropwise (1 drop per second) to the alkaline solution under stirring and maintained for 15 min at room temperature. Then, the magnetic stir bar was removed, and the Teflon bottle was transferred to a stainless-steel autoclave, sealed, and submitted to thermal treatment at 110 °C for 24 h in a preheated furnace. After the period, the autoclave was removed from the furnace and naturally cooling down at room temperature. The supernatant was removed and the obtained solid was washed five times with Milli-Q water and twice with ethanol at 10,000 rpm for 10 min in a centrifuge. The ethanol wash step is used to improve the drying process at 120 °C for 2 h (Fig. S1A).

2.3 Synthesis of Ni/CeO_2 via incipient wet impregnation

The impregnation of Ni onto CeO_2 nanowires was carried out using a wet impregnation method [18]. Initially, 2.0 g of CeO_2 nanowires were dispersed in 36.6 mL of Milli-Q water and ultrasonicated for 15 min to well disperse the CeO_2 nanowires. Then, 13.4 mL of an aqueous solution of $Ni(NO_3)_2{\cdot}6H_2O$ at 25.0 mM was added to the suspension under magnetic stirring. In sequence, the mixer was heated at 80 °C under stirring until all water was evaporated. The solid was dried at 120 °C for 2 h and calcined in air at 450 °C for 2 h (Fig. S1B).

2.4 Synthesis of Ni/CeO_2 via nanoparticles impregnation

The nanoparticles impregnation method was also employed for the impregnation of preformed Ni nanoparticles onto CeO_2 nanowires. Initially, 500 mL of an aqueous PVP solution at 0.5 M was stirred magnetically at 40 °C for 10 min in a round-bottomed flask immersed in an oil bath to achieve a homogeneous temperature solution. Subsequently, 13.4 mL of an aqueous $Ni(NO_3)_2{\cdot}6H_2O$ solution at 25 mM were added to the solution, followed by the carefully one-shot addition of 46.5 mL of a fresh aqueous $NaBH_4$ solution at 0.1 M, and the mixture was stirred at 40 °C for 4 h. After synthesizing the Ni nanoparticle, the suspension was added dropwise (1 drop per second) into a suspension of 2.0 g CeO_2 nanowires in 10.0 mL water and 10.0 mL ethanol under stirring at room temperature. The ethanol helps to avoid bobble formations due to the presence of PVP. After completing the addition, the reaction medium was stirred at room temperature for 4 h, the solid was washed five times with Milli-Q water and twice with ethanol at 10,000 rpm for 10 min in a centrifuge. Then, the solid was dried at 110 °C for 2 h and calcined in air at 450 °C for 2 h (Fig. S1C) [68].

2.5 Synthesis of Ni/CeO_2 via urea deposition method

The deposition of Ni nanoparticles on CeO_2 nanowires was carried out using a deposition-precipitation method assisted by urea [67]. In a round-bottomed flask, 2.0 g CeO_2 nanowires was dispersed in 100.0 mL Milli-Q water and ultrasonicated for 15 min. Then, the suspension was stirred magnetically for 15 min at 90 °C in an oil bath. Subsequently, 0.6 g urea was added to the suspension and 13.4 mL of an aqueous $Ni(NO_3)_2{\cdot}6H_2O$ solution at 25 mM was added dropwise (1 drop per second), and maintained under stirring at 90 °C for 4 h. After the period the glassware was removed from oil bath to naturally cooling down at room temperature. The solid was washed five times with Milli-Q water and twice with ethanol at 10,000 rpm for 10 min in a centrifuge. The solid was dried at 120 °C for 2 h and calcined in air at 450 °C for 2 h (Fig. S1D).

2.6 Synthesis of Ni/CeO_2 via $NaBH_4$ deposition method

The deposition of the Ni nanoparticles onto CeO_2 nanowires was carried out using a chemical reduction method assisted by $NaBH_4$ [69]. In a round-bottomed flask, 2.0 g CeO_2 nanowires were dispersed in 100 mL of a PVP/ethylene glycol solution at 1.3 g L^{-1} and ultrasonicated for 15 min. Then, the glassware was immersed in an oil bath at 90 °C for 15 min under magnetic stirring with a condenser trap to maintain a constant the concentration and volume of the reaction. Subsequently, 13.4 mL of an aqueous $Ni(NO_3)_2{\cdot}6H_2O$ solution at 25 mM was added to the mixture and 30.0 mL of a fresh $NaBH_4$ aqueous solution at 120.0 mM were one shot carefully added to the mixture and stirred at 90 °C for 4 h with a condenser trap to maintain a constant the concentration and volume of the reaction. After the period, the glassware was removed from the oil bath to cool down at room temperature. The solid was washed five times with Milli-Q water and twice with ethanol at 10,000 rpm for 10 min in a centrifuge. The solid was dried at 120 °C for 2 h and calcined in air at 450 °C for 2 h (Fig. S1E).

2.7 Characterization methods

Scanning electron microscopy (SEM) images were obtained using a JEOL Neoscope JCM-5000 field emission gun microscope operated at 5 kV. The samples were not pretreated before SEM analysis. The samples were dispersed in a mixture of 50% ethanol/water and ultrasonicated for 15 min. Then, the suspension was drop-casting the nanostructures over a silicon wafer and drying under ambient conditions. Before SEM analysis, the silicon wafer was washed with aquaria to prevent contamination.

Transmission Electron Microscopy (TEM) images were obtained with a JEOL JEM 2100 microscope operated at 200 kV. Before TEM analysis, the catalysts were treated under a H_2 atmosphere at 450 °C for 1 h under a flow rate of 50 mL·min^{-1}. After that, the catalysts were passivated under oxygen (O_2) (5%) diluted in a helium (He) atmosphere at 25 °C for 12 h under a flow rate of 50 mL·min^{-1} to emulate the catalytic reaction condition. After that, the samples were dispersed in a 50% ethanol/water mixture and ultrasonicated for 15 min. The suspension was drop-cast over a carbon-coated copper grid, followed by drying under ambient conditions.

Energy Dispersive X-ray Spectroscopy (EDS) is used for elementary maps using a Tescan VEGA 3 LMU scanning electron microscope operated at 20 kV equipped

with an Oxford detector with a 20 mm window. Samples were prepared by drop-casting an aqueous suspension containing the nanostructures over a silicon wafer, then drying under ambient conditions. Before EDS analysis, the silicon wafer was washed with aqua regia to prevent contamination.

Atomic Absorption Spectrometry (AAS) measured the Ni mass fractions using a ContrAA 300 Analitk Jena. Typically, 0.1 g of a catalyst was dissolved in an aqua regia solution (chloridric acid : nitric acid = 3 : 1) at 150 °C. After that, the sample was swelled to 50.0 mL with an HCl at 1.0 M and NH_4Cl at 0.1 M solution.

Thermogravimetric (TGA) measurements were carried out using a HITACHI STA 7300 equipment in the range of 25 –1000 °C using a heating rate of 10 °C·min^{-1} under air flow.

The X-ray diffraction (XRD) data were obtained using a Rigaku Miniflex X-Ray diffractometer and Cu K-alpha radiation (λ = 1.5418 Å). The diffraction patterns were obtained between Bragg's angle of 20° to 90° with a 0.05° min^{-1} angular speed scan. The diffractograms were analyzed with the aid of crystallographic files from the JCPDS database (Joint Committee on Powder Diffraction Standards) of the JADE 5 software.

Specific surface area, average pore diameter, and pore volume were determined by physisorption of N_2 at − 196 °C (77 K) in a Micromeritics ASAP 2020. Typically, 0.5 g of catalyst was pretreated under a 1.10^{-6} mmHg vacuum at 300 °C for 24 h. The adsorption and desorption isotherms were obtained by plotting the N_2 amount assimilated by the material as a function of the partial pressure. The specific areas were estimated by the Brunauer-Emmett-Teller model (BET method), and average pore diameter and pore volume were calculated by the Barret-Joyner-Halenda model (BJH method).

Raman spectra were collected using a in a Renishaw InVia Reflex coupled to a Leica DM 2500 M microscope and a CCD detector. The laser excitations used were 632.8 nm (He/Ne source) and the objective was a 50 × objective (NA = 0.9).

Temperature-programmed reduction with hydrogen (H_2-TPR) was carried out in a multipurpose unit with a Pfeiffer Vaccum Prisma detector mass spectrometer. Typically, 0.1 g of a catalyst was dried with He flow at 300 °C for 1 h and then cooled down to room temperature. The TPR profiles were obtained between 30 °C and 1000 °C in a flow of 2% H_2/He, at a rate of 10 °C·min^{-1}. H_2 consumption is calculated using H_2-TPR by comparing the reduction to a standard copper oxide.

H_2 chemisorption was carried out in a multipurpose unit with a mass spectrometer Pfeiffer Vaccum Prisma detector. Typically, 0.1 g of a catalyst was reduced with H_2 flow at 450 °C for 1 h, then kept under He flow for 30 min and cooled down to room temperature. H_2 was titrated in the catalysts until it did not present chemisorption.

Temperature-programmed desorption with H_2 (H_2-TPD) was carried out in a multipurpose unit with a Pfeiffer Vaccum Prisma detector mass spectrometer. After H_2 chemisorption, the temperature-programmed desorption was performed by heating in a stream of He at 50 mL·min^{-1} between 50 °C and 1100 °C with a heating rate of 10 °C·min^{-1}.

X-Ray photoelectron spectroscopy (XPS) data of the samples was obtained with a SPECSLAB II (Phoibos-Hsa 3500 150, 9 channeltrons) SPECS spectrometer, with Al Kα source (E = 1486.6 eV) operating at 12 kV, pass energy (Epass) = 40 eV, 0.1 eV energy step and acquisition time of 1 s per point. The samples were placed on stainless steel sample-holders and transferred under an inert atmosphere to the XPS pre-chamber and held for 2 h in a vacuum atmosphere. The residual pressure inside the analysis chamber was ~ 1 × 10^{-9} Torr. The binding energies (BE) of the Ce 3d and O 1s spectral peaks were referenced to the C 1s peak, at 284.5 eV, providing accuracy within ± 0.2 eV. The binding energies were calibrated by using the containment carbon (C1s = 284.6 eV) and the data was carried out using Fityk software with Gaussian function. Atomic Ce^{3+} concentration is calculated by XPS via the integration of the areas of the individual peaks to obtain the total area of the Ce^{3+} (Eq. 1) and Ce^{4+} (Eq. 2) [70]. The determination of surface oxygen was done via Eq. 3, where O_S is the surface oxygen, O_W is the adsorbed water, and O_L is the lattice oxygen [18, 19, 71–74]. The determination of surface Ni was done via Eq. 4, where Ni_S is the surface nickel, Ni_{Non} is the nonlocal nickel, and Ni_B is the bulk nickel [75–79].

$$\% \, Ce^{3+} = \frac{A_{Ce^{3+}}}{(A_{Ce^{3+}} + A_{Ce^{4+}})} \tag{1}$$

$$A_{Ce^{4+}} = U + U'' + U''' + V + V'' + V''' \tag{2}$$

$$\% \, O_S = \frac{A_{O_S}}{(A_{O_S} + A_{O_L})} \tag{3}$$

$$\% \, Ni_S = \frac{Ni_S}{(Ni_{Non} + Ni_S + Ni_B)} \tag{4}$$

2.8 Catalytic experiments: ethanol steam reforming

Catalytic experiments were conducted at atmospheric pressure in a fixed-bed quartz tubular reactor with a 5 mm inner diameter. The reactor was packed with quartz wool and 30, 50, or 100 mg of catalyst powder, resulting in bed heights of 1, 3, and 5 mm, respectively. The reactor was placed in a vertical oven equipped with a thermocouple to control the

temperature at 600 °C. Before reaction, the catalysts were reduced under pure H_2 atmosphere at 400 °C for 1 h, at a flow rate of 50 mL·min^{-1}. The reduction temperature was determined through the H_2–TPR (Fig. S3). Water and ethanol (CH_3CH_2OH) steams were generated using two bubblers: one containing water and the other ethanol, to obtain a H_2O/CH_3CH_2OH molar ratio of 3 and fed into the reactor. The feed composition (assessed via ethanol vapor pressure, P_{feed}) was determined by Antoine equation (Eq. 5) with parameters: water ($A = 4.65$, $B = 1435.26$, $C = -64.85$, and $T = 65$ °C) and ethanol ($A = 5.37$, $B = 1670.41$, $C = -40.19$, and $T = 15$ °C), and Raoult's law (P_{atm} = 1.01325 bar) (Eq. 6). The He inlet flow rates of the individual gas streams were controlled with mass flow meters (MKS Instruments) ranging from 10 to 80 mL·min^{-1} to ethanol and from 23 to 181 mL·min^{-1} to water, obtain a total flow rate from 33 to 265 mL·min^{-1}. At 33 mL·min^{-1} and 100 mg of catalyst were used to conventional literature experiment (contact time (W/F) of 3 mg·min·mL^{-1}, Fig. S4) [18, 67, 80, 81]. At 261 mL·min^{-1} with 30, 50, and 100 mg of catalyst were used to contact time experiments (contact time (W/F) of 0.11, 0.19, and 0.39 mg·min·mL^{-1}, Fig. S5). At 261 mL·min^{-1} with 50 mg of catalyst were used to deactivation experiments (contact time (W/F) of 0.19 mg·min·mL^{-1}, Fig. 6). The reactants and the reaction products were analyzed by gas chromatography (GC-2014 Shimadzu) equipped with two columns. The first column was a RQTPlot-Q (30 m, 0.32 mm i.d.) that separated the heavier products before being analyzed by an FID. Some lighter compounds, mainly H_2, CO and CO_2, are not detectable by the FID, such that the FID outlet stream was treated in a cold trap and then injected into another column (Carboxen 1010, 30 m, 0.53 mm i.d.) and then into a TCD. The tubes were kept at 120 °C, monitored by thermocouples to several sections to prevent condensation, fouling, and cold spots. Data processing was carried out by the software related to the chromatograph (GCSolution, v. 2.32), which provided online measurements of the catalytic performance.

$$logP_{feed} = A - \frac{B}{T + C} \tag{5}$$

$$P_{feed} = X_{feed} * P_{atm} \tag{6}$$

The analytic calibration curve was determined for ethanol (CH_3CH_2OH), hydrogen (H_2), carbon dioxide (CO_2), carbon monoxide (CO), methane (CH_4), acetone ($CH_3(CO)CH_3$), acetaldehyde (CH_3CHO), ethene (C_2H_4), ethane (C_2H_6), propene (C_3H_6), and propane (C_3H_8). The calibration curve was established using 5 points. The liquids were calibrated using a bubbler and the mole fraction was adjusted by varying the bubbler temperature determine via Antoine equation (Eq. 5), Raoult's law (Eq. 6), and Ideal gas law. Additionally, the molar fraction of the gases was adjusted by diluting them with the He carrier gas. The catalytic performance was evaluated by the conversion profiles of ethanol (X_{EtOH}) as in Eq. 7, where X_{EtOH} is the observed ethanol conversion given respectively the inlet ($mol_{EtOH,in}$) and outlet ($mol_{EtOH,out}$) ethanol flow rates. Selectivity for the obtained products (S_i) was evaluated as a function of the reaction time as in Eq. 8, where S_i refers to the product distribution of species i and C_i is the concentration of species i. The denominator represents the sum of the concentrations of every detected species n in the reactor outlet, like hydrogen (H_2), carbon dioxide (CO_2), carbon monoxide (CO), methane (CH_4), acetone ($CH_3(CO)CH_3$), acetaldehyde (CH_3CHO), and ethene (C_2H_4). The yield of i species (Y_i) is the product of ethanol conversion and species selectivity as described by Eq. 9.

$$X_{EtOH}\,[\%] = \frac{\left(mol_{EtOH,\ in} - mol_{EtOH,\ out}\right)}{mol_{EtOH,\ in}} \times 100 \tag{7}$$

$$S_i\,[\%] = \frac{C_i}{\sum_{m=1}^{n} C_p} \times 100 \tag{8}$$

$$Y_i\,[\%] = X_{EtOH} * S_i \tag{9}$$

3 Results and discussion

The study started with the synthesis of CeO_2 nanowires and Ni/CeO_2 nanowires catalysts employing various methods to produce Ni nanoparticles on CeO_2 nanowires. In the initial step, well-defined CeO_2 nanowires with specific shape and size were synthesized through a straightforward and robust procedure based on the hydrothermal method [19], as illustrated in Fig. S1A. The CeO_2 nanowires were formed in a single step: initially, the precursor salt solution underwent precipitation upon contact with the alkali solution under vigorous stirring, forming a precipitate complex (Eq. 10). Subsequently, inside a stainless-steel autoclave, the increased temperature and pressure enhanced the reactivity of the reaction medium, creating a favorable environment for hydrothermal treatment. This treatment decomposed the Ce complex, facilitating the growth of CeO_2 nanowires (Eq. 11). The obtained CeO_2 nanowires, as shown in Fig. S2, exhibited a narrow particle size distribution according to SEM and HRTEM images, and particle size distribution. The triplicate SEM images showed measurements of 15.4 nm ± 0.6 nm, 15.5 nm ± 0.8 nm, 15.2 nm ± 1.2 nm, with an average width of 15.3 nm ± 1.1 nm and a length of a few micrometers. Each batch was synthesized with a high yield of 97%, roducing around 2.8 g of CeO_2 nanowires. The first triplicate of the CeO_2 nanowires, which exhibited the narrowest particle

size distribution, was used in the following analysis. In the high-resolution transmission electron microscopy (HRTEM) image of an individual CeO_2 nanowire, the lattice fringes revealed a monocrystalline structure with interplanar spaces of 0.30 nm, corresponding to a uniform growth direction along the [82] axis [19, 83–85].

$$4Ce^{3+} + 4(y-1)OH^- + (4x+2)H_2O + O_2 \rightarrow 4\left[Ce(OH^-)_y\left(H_2O\right)_x\right]^{(4-y)+} \quad (10)$$

$$4\left[Ce(OH^-)_y\left(H_2O\right)_x\right]^{(4-y)+} + 4(y-1)OH^- \rightarrow CeO_2 + (x+2)H_2O \quad (11)$$

In the second step, with a focus on achieving well-dispersed Ni on the support, CeO_2 nanowires were chosen as a high surface area support to incorporate Ni using four different synthesis methods. The objective was to visualize and analyze the influence of each method on the properties of Ni nanoparticles and their consequence in surface reactivity. Figure 1 presents Scanning Electron Microscope (SEM), Transmission Electron Microscope (TEM), High-Resolution Transmission Electron Microscope (HRTEM), and Energy Dispersive X-ray Spectroscopy (EDS) map images of Ni/CeO_2 nanowires reduced under the same pretreatment conditions before catalytic experiments and passivated. In the first column, SEM images of Ni/CeO_2 nanowires indicate that the different synthesis methods do not influence the morphology and size of the CeO_2 nanowires, demonstrating the robustness of the synthesis. The second and third columns display TEM and HRTEM images of Ni/CeO_2, revealing the Ni nanoparticles. The fourth column presents the elemental distribution of Ni, Ce, and O through EDS. The scale bar in the EDS maps is equivalent to 2 µm.

The first two synthesis methods are impregnation techniques, involving the incorporation of the Ni^{2+} salt ($Ni(NO_3)_2$) precursor and preformed nanoparticles onto the CeO_2 nanowires through the adsorption of Ni^{2+} on CeO_2 nanowires. In the first method, illustrated in Fig. S1B, Ni was added through a wet impregnation route, known for its effectiveness in achieving high metallic dispersion on the support surface by producing a thin Ni layer on CeO_2 nanowires. Figure 1A-G display the results for Ni/CeO_2 wet impregnation, revealing a Ni monolayer on the CeO_2 nanowires, with lattice fringes at a distance of 0.30 nm corresponding to CeO_2 nanowires. Additionally, EDS mapping images demonstrate the incorporation of a thin Ni monolayer onto the CeO_2 nanowires.

The second impregnation method, depicted in Fig. S1C, involves initially producing Ni^0 nanoparticles through chemical reduction by $NaBH_4$ (Eq. 12) via homogeneous nucleation [86]. Subsequently, the Ni nanoparticles are incorporated onto CeO_2 nanowires through nanoparticle impregnation via adsorption between the metal and the support. Figure 1H-N illustrate Ni/CeO_2 nanoparticles impregnation, where the Ni nanoparticles exhibit a quasi-spherical shape with a diameter of 4.6 nm ± 0.3 nm and are well-dispersed on the CeO_2 nanowires.

The other two synthesis methods involve deposition techniques where Ni nanoparticles heterogeneously nucleate and grow on the CeO_2 nanowires through a chemical reaction. The third method, illustrated in Fig. S1D, is based on deposition-precipitation using urea, exploiting the reduction potential of Ni ($\Delta E°$ = -0.26 V). In this method, urea is hydrolyzed to form OH^- (Eq. 13) [86], which precipitates the Ni^{2+} ions as $Ni(OH)_2$ (Eq. 14). At a 90 °C in aqueous medium, urea is quickly hydrolyzed, changing the reaction color from light yellow, due to the CeO_2 nanowires dispersed, to black when in contact with Ni^{2+} ions, due to the Ni nanoparticles deposited on the surface of CeO_2 nanowires, as depicted in Fig. 1O-U. The Ni nanoparticles have a size of 12.9 nm ± 4.5 nm and a polydisperse shape. In Fig. 1P, some smaller Ni nanoparticles can be seen aggregating and merging into larger nanoparticles via the Ostwald ripening mechanism to minimize surface energy, likely due to heat treatment during calcination and/or pre-catalytic treatment. The small Ni nanoparticles formed as a result of the high temperature of the aqueous medium, which increased the hydrolysis rate and OH^- ions availability. The slow addition of Ni^{2+} ions promoted controlled precursor supply, leading to rapid deposition to the Ni nanoparticles nuclei without leaving remaining Ni^{2+} ions to grow.

The fourth and final method, illustrated in Fig. S1E, is based on the polyol method modified into deposition via chemical reduction by $NaBH_4$. In this approach, Ni^{2+} ions in the solution in ethylene glycol (EG) are reduced by BH_4^- to form Ni^0 metallic nanoparticles (Eq. 15) [87]. Figure 1V-AB illustrate the Ni/CeO_2 BH_4 deposition. The Ni nanoparticles exhibit a larger size of 36.8 nm ± 6.5 nm, attributed to the high reduction kinetics promoted by $NaBH_4$ and the lower nucleation energy required to deposit and nucleate the nanoparticles on the surface of CeO_2 nanowires. The lattice fringes of face-centered cubic (fcc) NiO (111) planes, approximately 0.21 nm, are evident in the Ni nanoparticles [88–91].

$$4Ni^{2+}{}_{(aq)} + BH^-_{4\,(aq)} + 3H_2O_{(l)} \rightarrow 4Ni_{(s)} + B(OH)_{3(aq)} + 7H^+{}_{(aq)} \quad (12)$$

$$CO\left(NH_2\right)_{2(aq)} + 3H_2O_{(l)} \rightarrow 2NH^+_{4\,(aq)} + CO_{2(g)} + 2OH^-{}_{(aq)} \quad (13)$$

$$Ni^{2+}{}_{(aq)} + 2OH^-{}_{(aq)} \rightarrow Ni(OH)_{2(s)} \quad (14)$$

$$2Ni^{2+}{}_{(eg)} + BH^-_{4\,(s)} + 2H_2O_{(eg)} + 2nPVP_{(eg)} \quad (15)$$

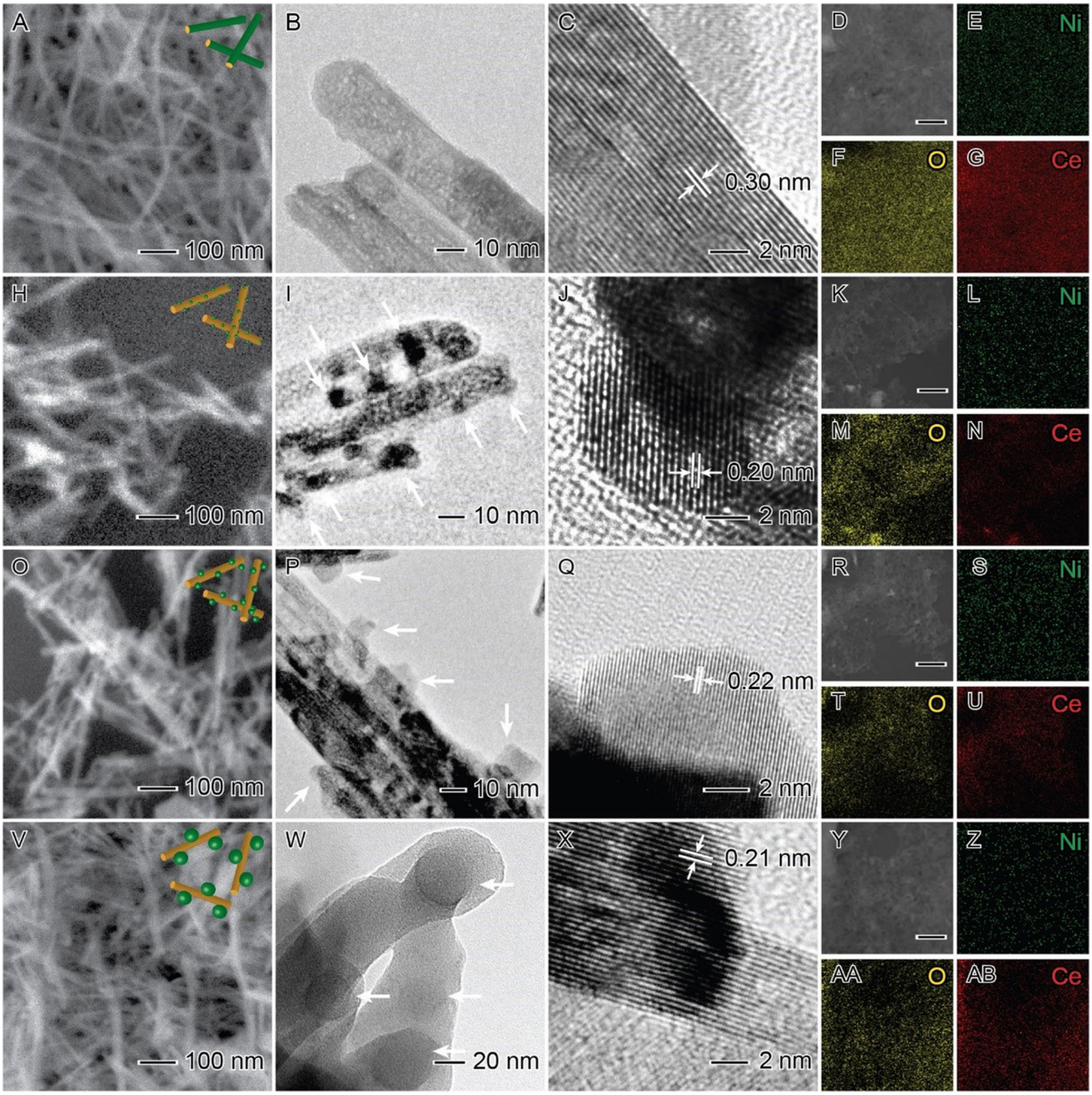

Fig. 1 SEM (First column), TEM (Second column), HRTEM (Third column), and EDS (Fourth column) images of Ni/CeO_2 nanowires synthesized via wet impregnation (**A-G**), nanoparticles impregnation (**H-N**), urea deposition (**O-U**), and BH_4 deposition (V-AB) methods. The scale bar in the fourth column is 2 µm. The white arrows in second column indicate the Ni nanoparticles

Table 1 summarizes the textural and physical-chemical properties of Ni/CeO_2 nanowires synthesized using different methods. Crystallite size was determined through X-Ray Diffraction (XRD), while HR-TEM and SEM provided particle size information. Specific surface area, average pore size, and average pore volume were obtained via N_2 physisorption using the BET and BJH models. Reducibility was assessed through temperature-programmed reduction with H_2 (H_2-TPR). H_2 chemisorption and H_2-TPD were utilized to determine metallic surface area, dispersion, H_2 adsorption, and desorption. Lastly, Ni content was measured using Atomic Absorption Spectroscopy (AAS). The XRD pattern, N_2 Isotherm, Raman spectra, H_2-TPR, and H_2-TPD of the samples are depicted in Figs. 2 and 3.

Table 1 The obtained catalysts' structural and surface properties were measured by XRD, HRTEM, N_2 physisorption, H_2-TPR, H_2 Chemisorption, H_2-TPD, and atomic absorption spectroscopy

	Crystallite Size (nm)	Particle Size (nm)	Specific Surface Area ($m^2 \cdot g^{-1}$)	Internal Surface Area ($m^2 \cdot g^{-1}$)	External Surface Area ($m^2 \cdot g^{-1}$)	Average Pore Size (Å)	Average Pore Volume ($cm^3 \cdot g^{-1}$)	Reducibility (%)	Specific Metal Surface Area ($m^2 \cdot g^{-1}$)	Ni Dispersion (%)	H_2 Adsorbed (μmol g^{-1}_{Ni})	H_2 Desorbed (μmol g^{-1}_{Ni})	Ni Content (mass fraction,%)
Ni/CeO_2 Wet Impregnation	21.7	--	42.5	12.6	29.9	237.6	0.25	52.2	125.4	42.4	36	66	0.91
Ni/CeO_2 Nanoparticles Impregnation	22.4	4.6	41.3	9.6	31.7	219.1	0.28	49.1	41.1	16.6	13	267	1.0
Ni/CeO_2 Urea Deposition	23.8	12.9	51.8	16.6	35.2	289.6	0.38	52.5	127.2	46.8	35	277	0.89
Ni/CeO_2 BH_4 Deposition	20.2	36.8	56.2	16.0	40.2	252.4	0.35	27.3	64.6	23.7	19	269	0.95
CeO_2 Nanowires	15.3	15.6	45.2	13.0	32.2	323.0	0.36	27.3	--	--	--	--	--

After synthesizing and confirming the morphology and size of the nanoparticles, the Ni amount incorporated in Ni/CeO_2 nanowires was quantified by AAS, as shown in Table 1. The Ni mass fractions in Ni/CeO_2 catalysts correspond to 0.91%, 1.0%, 0.89%, and 0.95% for Ni/CeO_2 wet impregnation, nanoparticles impregnation, urea deposition, and BH_4 deposition, respectively. The AAS data demonstrate the capability of the synthesis methods to decorate the metal on the support.

XRD profiles presented exhibit well-defined peaks assigned to their corresponding crystalline phases without contaminants. All the diffraction peaks (Fig. 2A) index to 2θ values of 28° (111), 33° (200), 47° (220), 56° (311), 58° (222), 69° (400), 76° (331), 79° (420), and 88° (422) planes, corresponding to a face-centered cubic (fcc) fluorite structure for CeO_2 [92]. After Ni incorporation, the XRD profiles for the Ni/CeO_2 catalysts changed due to thermal treatment and metal-support interaction, as evident in the crystallite size calculated using Scherrer's equation, which resulted in

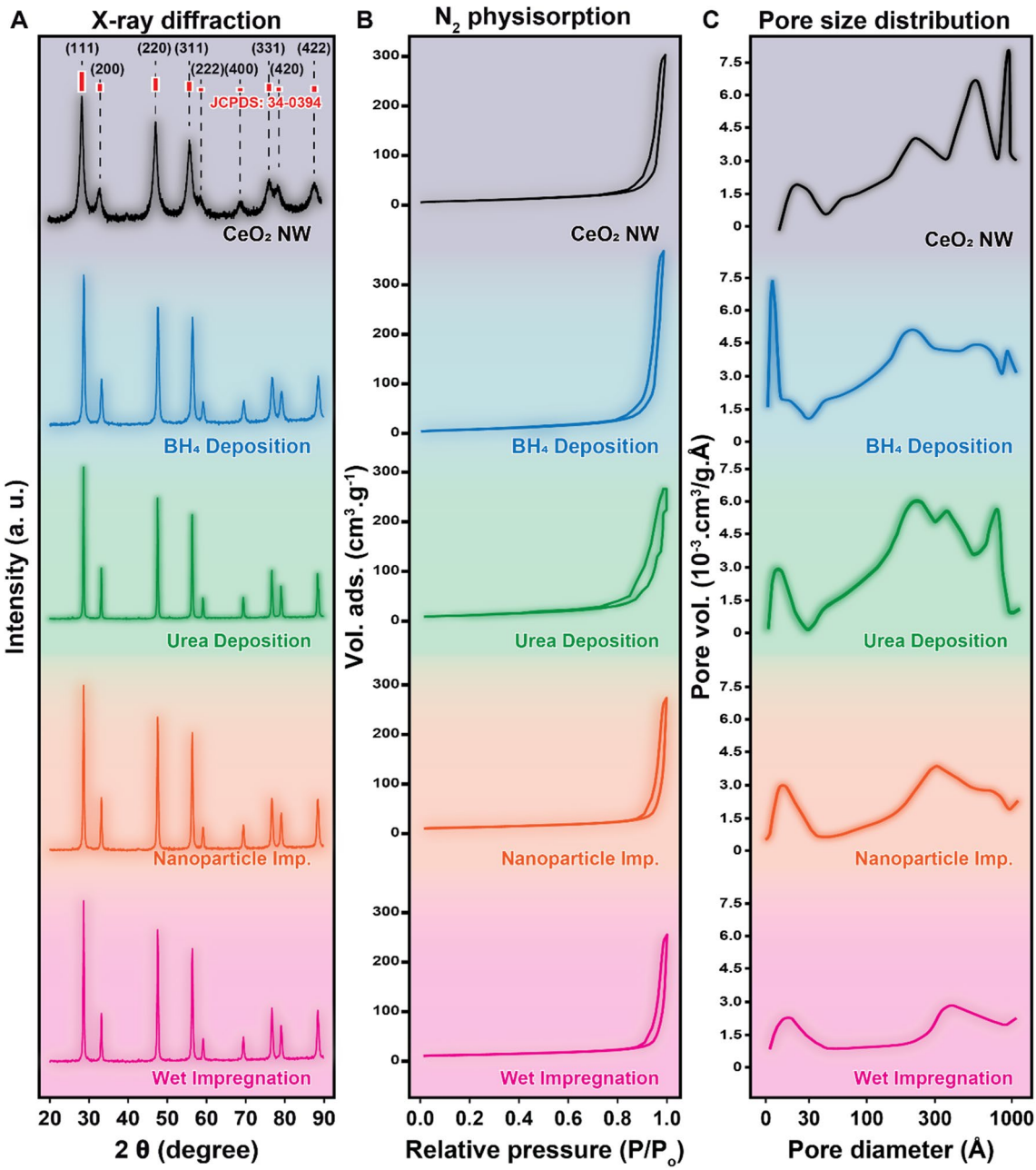

Fig. 2 XRD pattern (**A**), N_2 isotherms (**B**), and pore size distribution (**C**) for Ni/CeO_2 nanowires synthesized via impregnation and deposition methods, along with CeO_2 nanowires. In XRD pattern (A) is depicted the CeO_2 fcc fluorite structure JCPDS 34–0394

جامعة قطر
QATAR UNIVERSITY

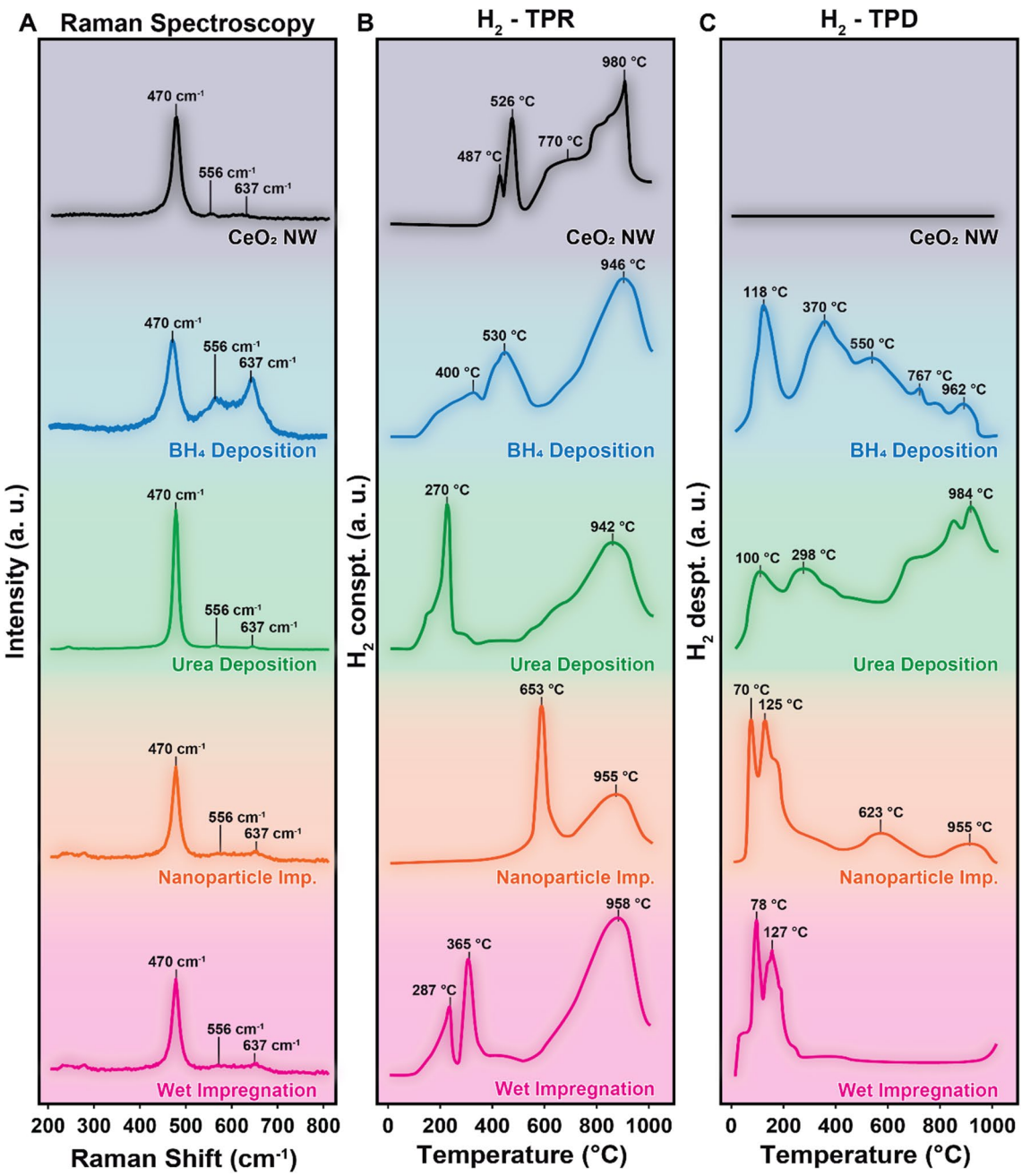

Fig. 3 Raman spectra (**A**), H_2-TPR (**B**), and H_2-TPD (**C**) for Ni/CeO_2 synthesized using different methods and CeO_2 nanowires

values of 21.7 nm, 22.4 nm, 23.8 nm, 20.2 nm, and 15.3 nm for Ni/CeO_2 wet impregnation, nanoparticles impregnation, urea deposition, BH_4 deposition, and pure CeO_2 nanowires, respectively.

It is worth noting that the difference between particle size measured by SEM microscopy and crystallite size in Table 1 is because microscopy measures the size of the whole nanoparticles and distinguishes the CeO_2 nanowires and Ni nanoparticles, while XRD measures the crystallite size. Furthermore, no peaks corresponding to Ni-based species were detected, which aligns with their small sizes and low Ni loadings in the samples. Additionally, as known, the scale decreases as the surface energy of a material increases due to the surface-to-volume ratio and the presence of dangling bonds, causing the contraction of the crystalline lattice in nanomaterials, which can be seen in CeO_2 nanowires crystallite size in Table 1 [67, 93, 94]. The incorporation of the metal on the support promotes metal-support interaction based on electron transfer and attractive forces. The equilibrium in the electron transfer satisfies the dangling bonds

and relax the tensioned bonds and increase the crystallite size [95, 96]. This phenomenon is depicted in Table 1, while incorporating Ni on the surface of the CeO_2 nanowires promotes an increment in the crystallite size of the Ni/CeO_2 nanowires, indicating a presence of metal-support interaction [95, 96].

Figure 2B; Table 1 present the N_2 adsorption-desorption isotherm curve of Ni/CeO_2 synthesized using different methods, CeO_2 nanowires, and detailed textural parameters. The isotherms of all catalysts exhibited II-type isotherms, characteristic of mesoporous materials, and the hysteresis loop shape corresponded to type H1 according to the IUPAC classification [19]. This corresponds to macropores that may be attributed to the aggregation of CeO_2 nanowires and a narrow range of uniform mesopores. A previous report by our group depicted TEM images of circular pores in CeO_2 nanowires with a diameter of ~2 nm and N_2 adsorption isotherm [19].

The catalysts exhibited specific surface areas, average pore sizes, and average pore volumes in the range of 32 to 56 $m^2 \cdot g^{-1}$, 219 to 323 Å, and 0.25 to 0.38 $cm^3 \cdot g^{-1}$, respectively. Moreover, the internal and external surface areas clarify the nanostructures disposal over both surfaces. These broad ranges are a consequence of the different sizes of Ni nanostructures. For instance, Ni/CeO_2 wet impregnation forms a thin layer, resulting in a specific surface area similar to that of CeO_2 nanowires. Here, internal surface is increased probably due to the formation of nanostructures with a rough surface inconsequence of a remained condensed Ni^{2+} solution into the pores. Ni/CeO_2 nanoparticles impregnation, being smaller in structure than other methods, shows lower values for textural properties, indicating potential nanoparticle blockage of pores. The internal surface area corroborates depicting that the Ni nanoparticles are filling the pores, and minor modifications in the external area in comparation of CeO_2 nanowires.

Ni/CeO_2 urea and BH_4 deposition methods produce intermediate and larger-sized Ni nanoparticles, contributing to higher specific surface areas. Figure 2C illustrates the pore diameter distribution for Ni/CeO_2 nanowires. The pore distribution in CeO_2 nanowires exhibits different pores with higher pore diameter, potentially corresponding to twisted CeO_2 nanowires. After Ni incorporation, a peak at a lower pore diameter increases to a narrow peak, suggesting that small nanoparticles block the pores and decrease the pore diameter. Moreover, both deposition methodologies show an increase in the external surface area, indicating that the Ni nanoparticles were beneficially deposited on the external surface.

Raman Spectroscopy is employed to determine the molecular structure and oxygen vacancies by analyzing molecular vibrational and rotational modes, providing a structural fingerprint for each system [97–99]. Figure 3A displays the Raman spectra normalized for Ni/CeO_2 and CeO_2 nanowires. CeO_2 exhibits an intense and narrow peak at 470 cm^{-1} associated with the fluorite structure in the F_{2g} mode. This peak is assigned to the symmetric stretching vibration of the eight oxygen atoms around Ce^{4+} ions due to the well-stoichiometric ratio [67]. The substitution of Ce^{4+} cations by Ce^{3+} causes an expansion of the lattice, leading to a broad and shifted F_{2g} peak at 556 cm^{-1}. Additionally, a low-intensity and broad peak at 638 cm^{-1} is related to oxygen vacancies produced by the reduction of cerium ions [19, 69]. The NiO spectra show two peaks at 556 cm^{-1} and 638 cm^{-1}, associated with the Raman symmetric stretching mode of Ni – O [100, 101]. However, as the CeO_2 and NiO exhibit a peak at 638 cm^{-1}, it is no able to verify the oxygen vacancies via Raman spectroscopy for Ni/CeO_2 nanostructures. Due to the low amount of Ni, small particle size, and high metal dispersion of Ni on the CeO_2 nanowire surfaces, the peaks attributed to the Ni nanoparticles exhibit low intensity for Ni/CeO_2 wet impregnation, nanoparticle impregnation, and urea deposition. However, Ni/CeO_2 BH_4 deposition, with a larger particle size, contributes to higher intensity peaks at 556 and 638 cm^{-1}, possibly indicating a higher concentration of oxygen vacancies.

The Temperature-Programmed Reduction with hydrogen (H_2-TPR) measures the reduction temperature and identifies the type and strength of the metal-support interaction in Ni/CeO_2 synthesized using different methods and CeO_2 nanowires. The reducibility of the CeO_2 nanowire support is a crucial parameter in catalytic applications, as metals can interact with metal oxides, altering their redox properties and influencing catalytic activity [71, 73, 102]. Pure CeO_2 typically exhibits two or three peaks related to the reduction of surface and bulk oxide. The first peak, occurring at temperatures below 500 °C, is linked to the reduction of surface oxide and active oxygen species. The second peak, typically observed in the temperature range between 500 °C and 650 °C, is attributed to the reduction of non-stoichiometric oxides with a composition of Ce_yO_x. The third and final peak occurs at temperatures higher than 800 °C and is associated with the bulk reduction of CeO_2 to Ce_2O_3 [71, 73, 102].

According to the literature, Du et al. describe that NiO exhibits two peaks during H_2-TPR analysis [103]. The first peak, ranging from 265 °C to 285 °C, is attributed to the reduction of weakly interactive NiO species with CeO_2 support. The second peak, observed at 360 °C to 380 °C, is related to the reduction of intensely interactive NiO species with CeO_2 support [101, 104]. Atzori et al. describe that NiO has two peaks [105]. The first peak is located at temperatures lower than 350 °C, ascribed to oxygen species reduction in oxygen vacancies generated by weak interaction with nickel. The locality of the second peak is at a temperature range between 400 °C and 600 °C, ascribed to the reduction of NiO species strongly interacting with CeO_2 [104–107].

Figure 3B; Table 1 present the H_2-TPR profiles of Ni/CeO_2 synthesized using different methods and CeO_2 nanowires, along with quantitative reducibility. CeO_2 nanowires exhibit two region peak temperatures between 400 °C and 600 °C and 600 °C and 1000 °C. The first region shows two peaks centered at 487 °C and 526 °C, corresponding to surface reduction of non-stoichiometric CeO_2 with active oxygen, surface Ce^{3+} ($Ce^{3+}-O-Ce^{4+}$), surface oxygen defects, and surface oxygen of stoichiometric CeO_2 ($Ce^{4+}-O-Ce^{4+}$). The second region displays two peaks at 770 °C and 980 °C, corresponding to the reduction of bulk CeO_2 [71, 73, 102]. For all Ni/CeO_2 synthesis methods, the second region is evident, with peak centers between 940 °C and 960 °C. However, the Ni/CeO_2 synthesis methods exhibit different temperatures for the first region, suggesting varying intensities of metal-support interaction due to the differences in synthetic methodologies [93].

The Ni/CeO_2 wet impregnation exhibited two peaks at 287 °C and 365 °C, corresponding to the reduction of NiO with weak interaction with the CeO_2 surface. Both peaks contribute to 52.2% of the reducibility. In contrast, Ni/CeO_2 nanoparticles impregnation displayed a single intense peak centered at 653 °C, indicating NiO reduction with strong interaction and 49.1% reducibility. Ni/CeO_2 urea deposition revealed a peak at 270 °C with 52.5% reducibility and weak interaction. Ni/CeO_2 BH_4 deposition exhibited two peaks at 400 °C and 530 °C, representing reductions of NiO with mild-strong interaction and reduction of the CeO_2 surface, contributing to 27.3% of the reducibility.

The difference in H_2-TPR profiles can be attributed to varying intensities of the metal-support interaction, influenced by differences in synthetic methodologies.

During wet impregnation, slow evaporation of the solvent facilitates the formation of a well-dispersed Ni thin film. This method promotes a minimized metal-support interaction, thereby exhibiting a weak interaction between Ni and CeO_2. In contrast, nanoparticles impregnation involves the adsorption of pre-formed small Ni nanoparticles onto the surface of CeO_2. This method does not chemically modify the CeO_2 surface and allows for a strong interaction between Ni nanoparticles and unmodified, strong negative oxygen vacancies, as observed in the CeO_2 nanowires profile. However, deposition methods involving chemical reactions to deposit Ni nanoparticles can modify the CeO_2 surface. Urea deposition results in uncontrolled nanoparticle formation, suggesting that Ni nanoparticles undergo an energy minimization mechanism, promoting a weak metal-support interaction. On the other hand, BH_4 deposition involves the reduction of Ni^{2+} ions, which can act as nucleation sites on the CeO_2 surface, leading to a moderate to strong metal-support interaction, as indicated by the H_2-TPR profile. These adjustments aim to clarify the influence of synthetic methods on the metal-support interaction in our study.

Figure S3 illustrates the H_2-TPR profiles with 2% H_2/He and pure H_2. The profiles remain consistent with a shift toward lower temperatures, with the peak corresponding to the reduction of bulk CeO_2 splitting into two peaks. The first may correspond to the reduction of the CeO_2 surface, and the second to bulk reduction. The reduction profile provides insights into the size of Ni nanoparticles. Wet impregnation, forming thin layers, results in weak metal-support interaction. Nanoparticle impregnation, with smaller sizes, leads to strong metal-support interaction, evident from the high-temperature peak. Urea deposition, potentially producing small-sized Ni nanoparticles with high surface energy, exhibits an early peak. In contrast, BH_4 deposition, with the largest nanoparticles, shows intermediate metal-support interaction.

The reduction of catalysts occurred under a pure H_2 flow rate, and H_2-TPR was carried out with diluted H_2, known to increase the reduction rate and potentially produce different phases. This approach aims to gain further insights into the catalyst under catalytic conditions. Figure S3 presents a comparison between the reduction profiles with diluted H_2 (Fig. S3A) and pure H_2 (Fig. S3B). The reduction profile remains consistent below 450 °C, with a slight shift of the two initial peaks at 287 °C and 365 °C to 218 °C and 272 °C. Notably, the reduction peak associated with CeO_2 at 958 °C splits into two peaks at 655 °C and 1,000 °C, possibly linked to the reduction of CeO_2 to Ce_2O_3, as reported in previous studies [71, 73, 102]. Moreover, it is important analyze Fig. S3B to determine the reduction temperature of the nickel oxides to metallic nickel nanoparticles, which the first reduction area ends at 400 °C.

Figure 3C; Table 1 present the Temperature-Programmed Desorption of hydrogen (H_2-TPD) for the Ni/CeO_2 synthesis methods, providing quantitative information on reducibility. H_2-TPD offers insights into variations in metal-support interactions. According to the literature, H_2 desorption peaks at low temperatures ($\leq$250 °C) are attributed to hydrogen species weakly bonded to active nickel sites [107, 108]. The temperature range between 250 °C and 450 °C is associated with strong bonding to nickel, while temperatures exceeding 450 °C indicate very strong chemisorption on the nickel surface [107, 108]. The H_2-TPD profiles for Ni/CeO_2 synthesis methods exhibit desorption peaks below 130 °C, corresponding to weak interactions. Peaks between 300 °C and 450 °C indicate strong interactions, and peaks above 450 °C suggest very strong interactions or may be related to nickel and other transition metals serving as hydrogen reservoirs. These metals can adsorb and store substantial amounts of hydrogen on the metal-support interface or as spilled-over species. The higher desorbed amounts of hydrogen than adsorbed amounts are attributed to H_2 molecules retained

on the Ni nanostructures during pretreatment, as depict in H_2 adsorbed and desorbed in Table 1 [82, 107–111].

The Ni/CeO_2 wet impregnation exhibited two desorption peaks at 78 °C and 127 °C, attributed to two different intensities of H-Ni interaction—very weak interaction and weak interaction, respectively. The Ni/CeO_2 nanoparticles impregnation exhibited four desorption peaks, including two intensity peaks at 70 °C and 125 °C, and two lower intensity peaks at 623 °C and 955 °C. The peaks at low temperatures are associated with very weak and weak interactions, while the peaks at high temperatures are associated with very strong interaction or H_2 retention.

The Ni/CeO_2 urea deposition exhibits three prominent peaks at 114, 337, and 984 °C. The peak at low temperature is associated with weak interaction, the intermediate peak is associated with strong interaction, and the high-temperature peak is associated with very strong interaction. When comparing impregnation methods, the first desorption peak can be associated with mild interaction, and the second desorption peak with strong interaction and H_2 retention.

Lastly, Ni/CeO_2 BH_4 deposition exhibits five desorption peaks at 118, 370, 550, 767, and 962 °C. Classical nickel-based catalysts typically show two or more peaks at different temperatures due to the formation of several active sites. The first peak can be associated with mild interaction, while the other peaks are associated with strong and very strong interaction, as well as H_2 retention. These results indicate that the impregnation methods result in weak H-Ni interaction at metal sites, and the impregnated catalysts desorb H_2 at low temperatures, demonstrating good H_2 lability. In contrast, the deposition methods show considerable H-Ni solid interaction at metal sites, indicating less favorable H_2 lability. It is possible that the catalysts prepared through deposition methods have higher interaction with H_2 on the active sites.

X-ray Photoelectron Spectroscopy (XPS) analyses (Fig. 4, Tables 2, and S1) were performed to identify surface composition and gain further insights into the Ni/CeO_2 different synthesis methods and CeO_2 nanowires. Figure 4 presents the Ce 3d (Fig. 4A), O 1s (Fig. 4B), and Ni 2p (Fig. 4C) core-level spectra for Ni/CeO_2 different synthesis methods and CeO_2 nanowires. The Ce 3d region exhibits two multiplets with ten peaks, where V and U indicate the spin-orbit coupling Ce $3d_{5/2}$ and Ce $3d_{3/2}$, respectively. The Ce 3d spectra consist of peaks assigned to Ce^{4+} and Ce^{3+} species on the surface. The peaks V, V'', V''', U, U'', and U''' correspond to the Ce^{4+} $3d^{10}$ $4f^0$ state, while V_0, V', U_0, and U' correspond to the Ce^{3+} $3d^{10}$ $4f^1$ state (Table S1) [19, 72, 73, 102].

When the dimensions of CeO_2 are reduced from the bulk to the nanoscale, the geometric and electronic parameters are influenced by the increased exposed atoms on the surface and the dangling bond. This promotes a lattice tension that raises the surface free energy [67, 93, 94]. Consequently, the high tension in the electrotonic structure and crystalline lattice creates an unfavorable environment for stoichiometric oxide [112, 113]. Unstable atomic bonds lead to the release of oxygen atoms, leaving an excess of electrons in the material. The release of oxygen atoms results in the formation of oxygen vacancies [2]. The electronic structure of the crystal is stabilized as empty levels capture of cation and redistribute the electrons resulting from the released oxygen. This process changes the oxidation state of cerium ions from Ce^{4+} to Ce^{3+} [2, 114–116]. The Ce^{3+} ions are distributed in regions of sesquioxide Ce_2O_3 around oxygen vacancies in CeO_2. XPS deconvolution and integration of the peaks are used to determine the atomic Ce^{3+} concentration [70]. Table 2 summarizes the surface composition of the Ni/CeO_2 different synthesis methods and CeO_2 nanowires. The percentage of Ce^{3+} onto the CeO_2 nanowires is 24.53%, and amount of Ce^{3+} increases withthe size.

To validate this observation, we examined the O 1s XPS spectra (Fig. 4B). The O 1s XPS spectra consist of three peaks representing lattice oxygen (O_L) between 531.2 and 530.3 eV, surface oxygen ions, or oxygen vacancies (O_S) between 532.2 and 531.9 eV, and adsorbed water (O_W) between 534.6 and 534.2 eV (Table S1) [19, 117]. The percentage of O_S in the samples, as shown in Table 2, reveals the proportion of surface oxygen in the samples [18, 19, 71–74]. It is important to note that the percentage of the O_S is the sum of surface oxygen in the CeO_2 nanowires and oxidized Ni nanoparticles as NiO.

The data indicates that the wet impregnation method does not extremely modify the surface of CeO_2 nanowires with the addition of Ni, as analyzed by the Ce^{3+} and O_S contentes. However, in the nanoparticle impregnation method, small Ni nanoparticles (4.6 nm) were adsorbed on the surface of CeO_2 nanowires, potentially occupying more electronic sites and promoting a strong metal-supporting interaction, as observed in the H_2-TPR and Ce^{3+} content. The deposition methods depicted a higher O_S content, suggesting a chemical interaction between nickel and support involving higher electron transfer or potential formation of a Ni−O−Ce spinel at the interface [118]. Additionally, larger Ni nanoparticles may have a higher amount of NiO on the surface.

Figure 4C displays the Ni $2p_{3/2}$ XPS spectra. The electronic structure of NiO can be described as a rearrangement of the Ni final state of the $3d^8$, $3d^9L$, and $3d^{10}L^2$ (where L denotes a hole in the ligand band and c denotes a Ni 2p core level hole) level of the electrons in the valence band configuration affected in photoemission [75–79]. The Ni $2p_{3/2}$ XPS spectra consist of four peaks corresponding to a configuration screened by an oxygen electron at the bulk cluster (Ni_B; red line; $c3d^9L$:$3d^8$), oxygen electron at the surface (Ni_S; green line; $3d^8$:$c3d^9L$), non-local electron coming from the neighboring Ni ion (Ni_i; blue; $c3d^9$:$3d^7$ and $3d^7$:$c3d^9$), and a satellite peak (cyan). The shifts in the Ni 2p spectra can be attributed to significant hydroxylation associated with

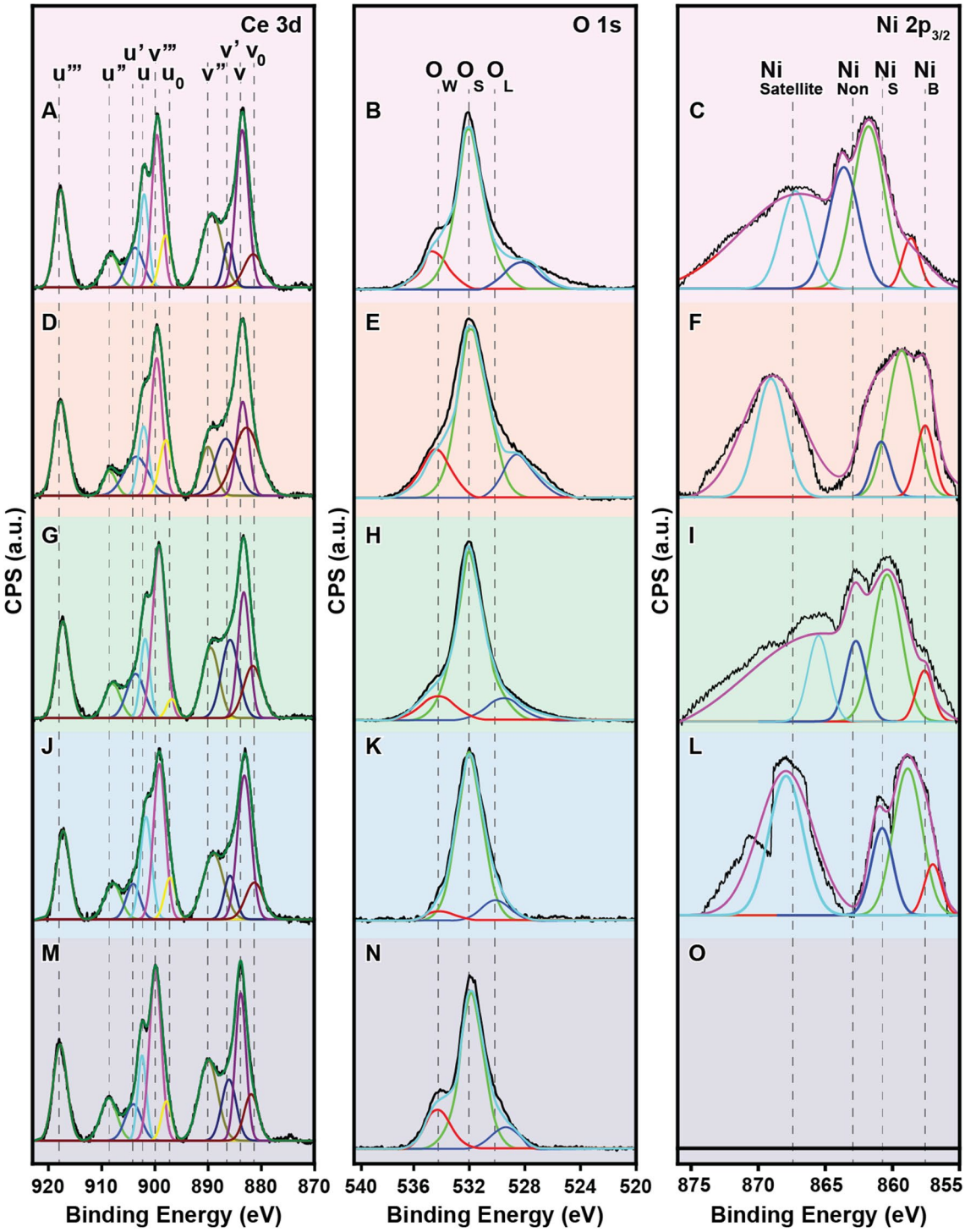

Fig. 4 XPS spectra of (**A**) Ce 3d, (**B**) O 1s, and (**C**) Ni 2p for Ni/CeO_2 synthesized using different methods and CeO_2 nanowires

the surface-state effects and residual charging [75–79]. As indicated in Fig. 3, the percentage of surface Ni increases with smaller nanostructures, as thin film to wet impregnation and 4.6 nm to nanoparticles impregnation, and is bigger nanoparticles, as urea and BH_4 depositions with 12.9 and 36.8 nm, respectively, from 35.48%, 36.30%, 3.85%, ad 29.12 .

Here, we understand that the Ni/CeO_2 nanomaterial has influenced the different synthesis methods to create four structures and nanoparticles of various sizes, affecting

Table 2 XPS parameters for Ce^{3+} content (at%), O_S content (at%), and Ni_S (%) were obtained from the ce 3d, O 1s, and Ni 2p regions for the Ni/CeO_2 different synthesis methods and CeO_2 nanowires

Sample	Ce^{3+} Content (at%)	O_S Content (at%)	Ni_S (%)
Ni/CeO_2 Wet Impregnation	23.27	81.08	35.48
Ni/CeO_2 Nanoparticles Imp.	44.32	79.71	36.30
Ni/CeO_2 Urea Deposition	30.60	87.66	30.85
Ni/CeO_2 BH_4 Deposition	22.64	94.17	29.12
CeO_2 Nanowires	24.53	81.39	--

different nickel properties such as reducibility, surface composition, oxygen vacancies, and metal-support interaction. It highlights the combination of exceptional properties makes possible the application of Ni/CeO_2 synthesized through different methods as an effective catalyst for ethanol steam reforming and potentially for many other reactions. Subsequently, following the synthesis and characterization of Ni/CeO_2 catalysts via various methods, our focus shifted to investigating their catalytic properties, performance, and the impact of synthesis methods on surface reactivity in ethanol steam reforming, as illustrated in Fig. 5A for the chemical reaction and depicted coproducts in Fig. 5C.

We conducted the catalytic experiments under the standard conditions reported in the literature: reactions were set with an H_2O/CH_3CH_2OH molar ratio of 3, using 100 mg of catalyst, at 600 °C, and with a gas flow of 32 mL·min^{-1}, to achieve a contact time (W/F) of 3 mg·min·mL^{-1} (Fig. S4) [18, 24, 67, 80, 81]. However, all catalysts exhibit 100% converion during the 24 h reaction period, which did not differentiate the influence of synthesis methods on the surface reactivity of these catalysts. To gain further insight into the surface reactivity of Ni/CeO_2 catalysts, the contact time (Weight / Flow rate) was reduced by 16 times, from 3.0 to 0.2 mg·min·mL^{-1}. Figure S5 illustrates the influence of contact time on the conversion and selectivity of Ni/CeO_2 catalysts. It is interesting to note that at the initial point of analysis, 5 min into the reaction, there is a minimal difference in ethanol conversion of 100% at 3 m·min·mL^{-1} (Fig. S4) and 97% at 0.1 mg·min·mL^{-1} (Fig. S5). These small differences in ethanol conversion indicate that the kinetic regime has not been reached and the catalysts are still in the diffusional regime.

To ensure data reliability, measurements were taken during low contact time reactions. Figure S6A displays the average and error distribution for conversion and selectivity of the Ni/CeO_2 wet impregnation catalyst triplicates (Fig. S6B-D). The consistent average conversion and selectivity, coupled with low error distribution, indicate reproducible catalytic experiments. Calculating the main error from the triplicate conversion during the 48 h catalytic test yielded a value of 1.6%.

The catalytic experiments were conducted at the maximum conditions supported by experimental catalytic system at 0.19 mg·min·mL^{-1} under a gas feed flow of 261 mL·min^{-1} and using 50 mg of catalyst. Figures 5 and 6 depict the ethanol conversion and selectivity for CeO_2 nanowires and Ni/CeO_2 nanowires, respectively. The catalytic test lasted 48 h, aiming to distinguish the activity performance and stability of the catalysts under various conditions. The CeO_2 nanowires revealed high ethanol conversion around 100% and stable selectivity throughout the entire reaction period. As expected, the CeO_2 nanowires exhibit higher selectivity to C_2 compounds, such as ethene, and lower selectivity to C_1 compounds, such as methane, and H_2 at higher contact times [119–121]. These data align with literature findings, as ethanol is adsorbed on the CeO_2 surfaces through dissociative adsorption in a dehydrogenation reaction to form adsorbed

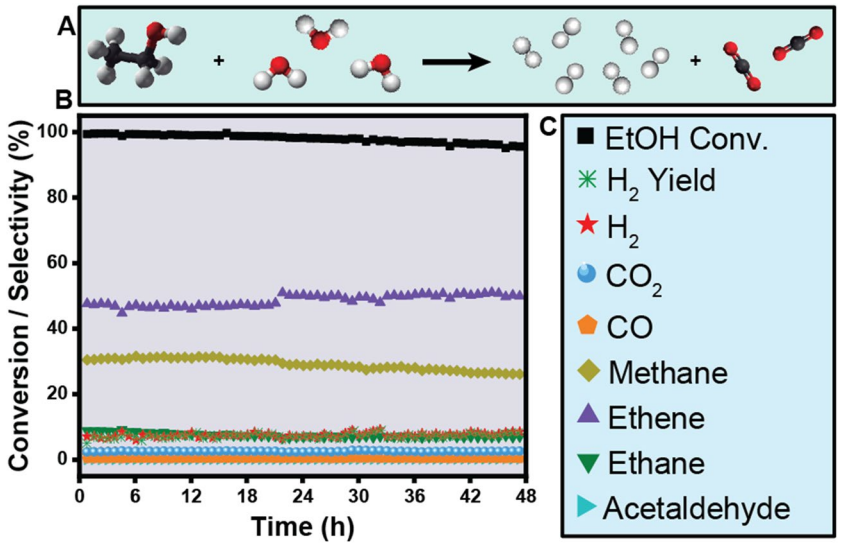

Fig. 5 Ethanol Steam Reforming catalytic test showing the ethanol conversion, selectivity, and H_2 yield is employing the CeO_2 nanowires. The experiments were performed at 600 °C, H_2O/CH_3CH_2OH molar ratio = 3, 50 mg of catalyst, and gas flow = 261 mL·min^{-1}

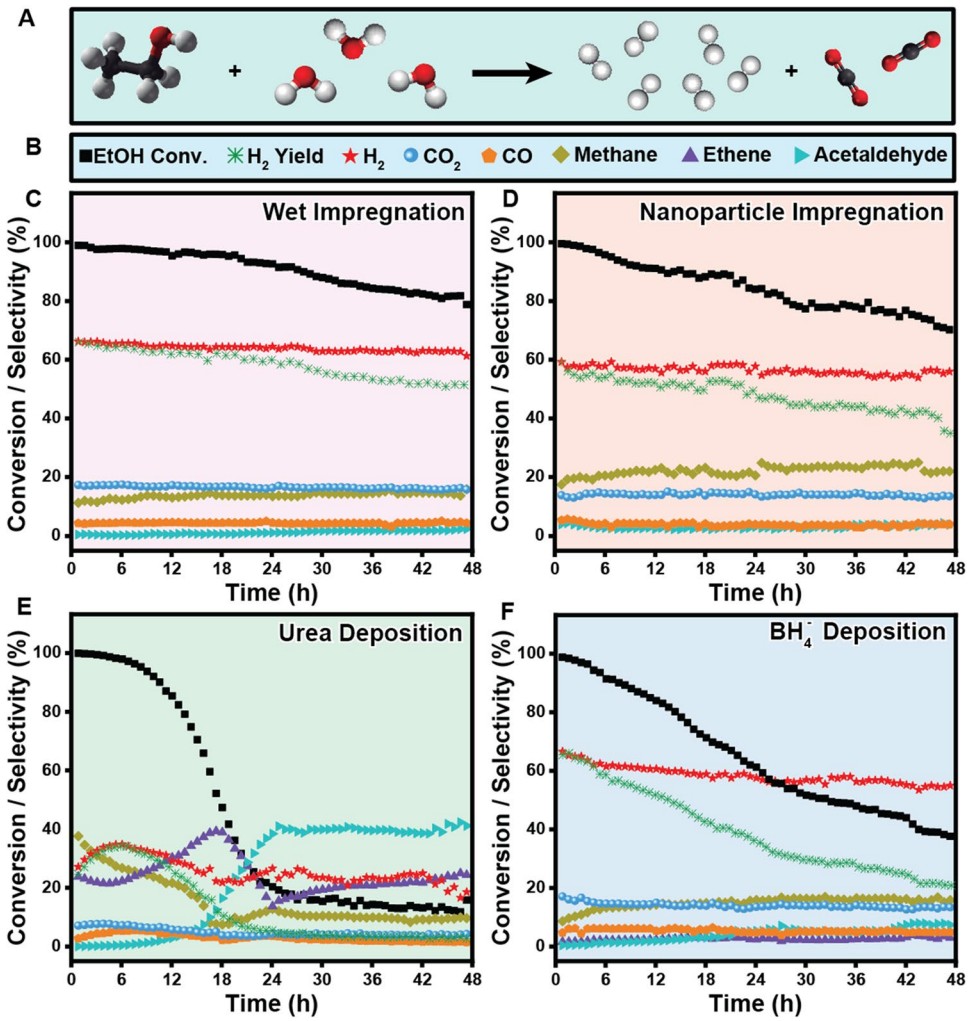

Fig. 6 Illustration of the ethanol steam reforming reaction (**A**), the reaction products (**B**), and catalytic reaction tests showing ethanol conversion, selectivity, and H_2 yield employing Ni/CeO_2 synthesized via wet impregnation (**C**), nanoparticle impregnation (**D**), urea precipitation deposition (**E**), and BH_4 reduction deposition (**F**). The experiments were performed at 600 °C, with a H_2O/CH_3CH_2OH molar ratio of 3, 50 mg of catalyst, and gas flow of 261 mL·min^{-1}

ethoxy ($CH_3CH_2OH \rightarrow CH_3CH_2O^* + H^*$), followed by the dehydroxylation of ethoxy to ethene ($CH_3CH_2O^* \rightarrow CH_2CH_{2(g)} + OH^*$) [119–121]. It is noteworthy that acetaldehyde can be adsorbed on the surface due to oxygen in the carbonyl group, while ethylene does not form a stable adsorption product and desorbs immediately [119, 120]. According to Mudiyanselage et al. [120], surface oxygen defects accelerate the ethanol reaction, explaining the high ethanol conversion for CeO_2 nanowires and corroborating the XPS data regarding the high oxygen surface content.

Here, after nickel incorporation onto the CeO_2 nanowires, the different synthesis methods of Ni/CeO_2 promoted the ethanol steam reforming reaction (Eq. 20 and depicted in Fig. 6A). It is notable that the different synthesis methods influenced the catalytic activity of Ni/CeO_2. The impregnation methods displayed a similar catalytic profile with high ethanol conversion and H_2 selectivity. Furthermore, at the end of the first 24 h, wet impregnation exhibits 6% deactivation, while nanoparticle impregnation exhibits 14% deactivation. After 48 h, Ni/CeO_2 wet impregnation (Fig. 6C) exhibited 20% deactivation and 61% H_2 selectivity, whereas Ni/CeO_2 nanoparticles impregnation (Fig. 6D) exhibited 27% deactivation and 55% H_2 selectivity. Both catalysts exhibit low selectivity for C_2 compounds, less than 3% for acetaldehyde and ethene, demonstrating high surface reactivity to completely follow the reaction pathway to final products. However, the deposition methods displayed strong deactivation and different reaction profiles. After 48 h of the experiment, Fig. 6E shows that the Ni/CeO_2 urea deposition catalytic profile exhibits 86% deactivation, low H_2 selectivity at 23%, and considerable selectivity towards acetaldehyde (39%) and ethene (23%). Figure 6F shows the Ni/CeO_2 BH_4 deposition catalytic profile, exhibiting strong deactivation (62%) but high H_2 selectivity (55%). However, the Ni/CeO_2 urea deposition depicts a change in the reaction mechanism. Initially, the mechanism focused on ethene, methane, and H_2 production. After strong deactivation, the mechanism shifts to acetaldehyde production.

Catalytic profiles are influenced by changes in active sites and the reducibility of catalysts. Wet impregnation resulted in two distinct peaks at lower temperatures (287 and 368 °C), indicative of strong metal-support interactions and enhanced

activity sites. Additionally, H_2-TPD analysis revealed merged desorption peaks at lower temperatures (78 and 127 °C), suggesting facile H_2 release, possibly due to well-dispersed Ni forming a thin film with uniform active sites. Nanoparticles impregnation exhibited a prominent reduction peak at higher temperature (663 °C), indicating weaker metal-support interactions and fewer active sites. Correspondingly, H_2-TPD showed smaller peaks at higher temperatures (623 and 955 °C), suggesting poor H_2 utilization and site deactivation. Urea deposition exhibited a reduction peak at a lower temperature (270 °C), signifying strong metal-support interactions and increased active sites. However, H_2-TPD showed a significant peak at higher temperatures (600 to 1,000 °C), indicating strong hydrogen interaction with active sites. These strong sites deactivated initially during catalyst testing, with lower intensity active sites operating in the subsequent mechanism [27, 122, 123]. BH_4 deposition displayed two merged peaks between 100 and 600 °C, indicative of non-uniform active sites, which was confirmed by H_2-TPD showing a range-like profile with multiple desorption peaks. In conclusion, utilizing H_2-TPR and H_2-TPD to estimate metal-support interactions and active sites reveals a trend where strong metal-support interactions lead to more active sites. However, the homogeneity and intensity of these active sites significantly influence catalytic behavior, with more intense desorption peaks at higher temperatures indicating faster deactivation compared to weaker desorption sites.

According to the literature, the ethanol steam reforming mechanism can change depending on factors such as adsorption energy, acidity and basicity of the catalyst, active metal, catalyst support, H_2O/ethanol ratio, and the ability of the active metal to cleave C–C, C–H, and C–O bonds [56, 124–126]. Essentially, the mechanism begins with the dissociative adsorption of ethanol in a dehydrogenation process forming adsorbed ethoxy ($CH_3CH_2OH \rightarrow CH_3CH_2O^*$). Then, ethanol can undergo decomposition (Eq. 16), dehydrogenation (Eq. 17), or dehydration (Eq. 18) to produce CH_4, CO, H_2, acetaldehyde, and ethene, respectively [127–130]. These products can either desorb or continue reacting. Ethene can further decompose into solid carbon and H_2 (Eq. 19) [123, 126]. Acetaldehyde may decompose to methane and CO (Eq. 20) or undergo steam reforming to produce H_2 and CO (Eq. 21) [131, 132]. Finally, several reactions involving C_1 compounds may occur, such as methanation (Eqs. 22 and 23), water gas shift (Eq. 24), carbon hydrogenation (Eq. 25) (references [133, 134]), and methane steam reforming (Eq. 26), among others [128, 133].

$$C_2H_5OH_{(ads)} \rightarrow CH_{4(g)} + CO_{(g)} + H_{2(g)} \tag{16}$$

$$CH_3CH_2OH_{(g)} \rightarrow CH_3CHO_{(g)} + H_{2(g)} \tag{17}$$

$$CH_3CH_2OH_{(g)} \rightarrow C_2H_{4(g)} + H_2O_{(g)} \tag{18}$$

$$C_2H_{4(ads)} \rightarrow 2\,C_{(s)} + 2H_{2(g)} \tag{19}$$

$$CH_3CHO_{(g)} \rightarrow CH_{4(g)} + CO_{(g)} \tag{20}$$

$$CH_3COH_{(ads)} + H_2O_{(ads)} \rightarrow 3H_{2(g)} + 2CO_{(g)} \tag{21}$$

$$3H_{2(g)} + CO_{(g)} \rightarrow CH_{4(g)} + H_2O_{(g)} \tag{22}$$

$$4H_{2(ads)} + CO_{2(ads)} \rightarrow CH_{4(g)} + 2H_2O_{(g)} \tag{23}$$

$$CO_{(ads)} + H_2O_{(ads)} \rightarrow CO_{2(g)} + H_{2(g)} \tag{24}$$

$$C_{(s)} + H_{2(ads)} \rightarrow CH_{4(g)} \tag{25}$$

$$CH_{4(ads)} + H_2O_{(ads)} \rightarrow CO_{(g)} + 3H_{2(g)} \tag{26}$$

The catalyst deactivation follows the trend: CeO_2 nanowires < wet impregnation < nanoparticles impregnation < BH_4 deposition < urea deposition, displaying deactivation of 3%, 20%, 27%, 62%, and 86%, respectively. The CeO_2 nanowires exhibited the lowest catalytic deactivation, likely because of its significant oxygen storage capability and oxygen mobility at the surface due to the presence of Ce^{3+} and Ce^{4+} ions. These ions are associated with preventing the deposition of solid carbon compounds at the active sites. This characteristic is evident in the XPS analysis, which shows that CeO_2 nanowires have 70% of oxygen on the surface. Furthermore, the oxygen vacancies at the surface likely adsorb ethanol via hydroxyls as part of the reaction mechanism, leading to the scission of the O – C bond to form ethene in high proportions, as depicted in ethene selectivity and yield. It is important to note that CeO_2 nanowires can help prevent catalytic deactivation in Ni/CeO_2. However, the metal-support interaction can alter the activity of CeO_2 nanowires.

After the catalytic experiments, all Ni/CeO_2 synthesized using different methods and CeO_2 nanowires catalysts were characterized by SEM images, XRD spectra, TGA profiles, and Raman spectra (Fig. 7). The SEM images (Fig. 7A-E) reveal that the overall sizes and shapes of Ni/CeO_2 and CeO_2 nanowires remained unchanged after 48 h of catalytic experiments at 261 mL·min^{-1}, 50 mg, and 600 °C. A careful analysis shows different amounts of carbon deposits on the surface of Ni/CeO_2 and CeO_2 nanowires. XRD analyses (Fig. 7F) indicate well-defined peaks assigned to CeO_2, suggesting that the overall structures of Ni/CeO_2 and CeO_2 nanowires remained unchanged

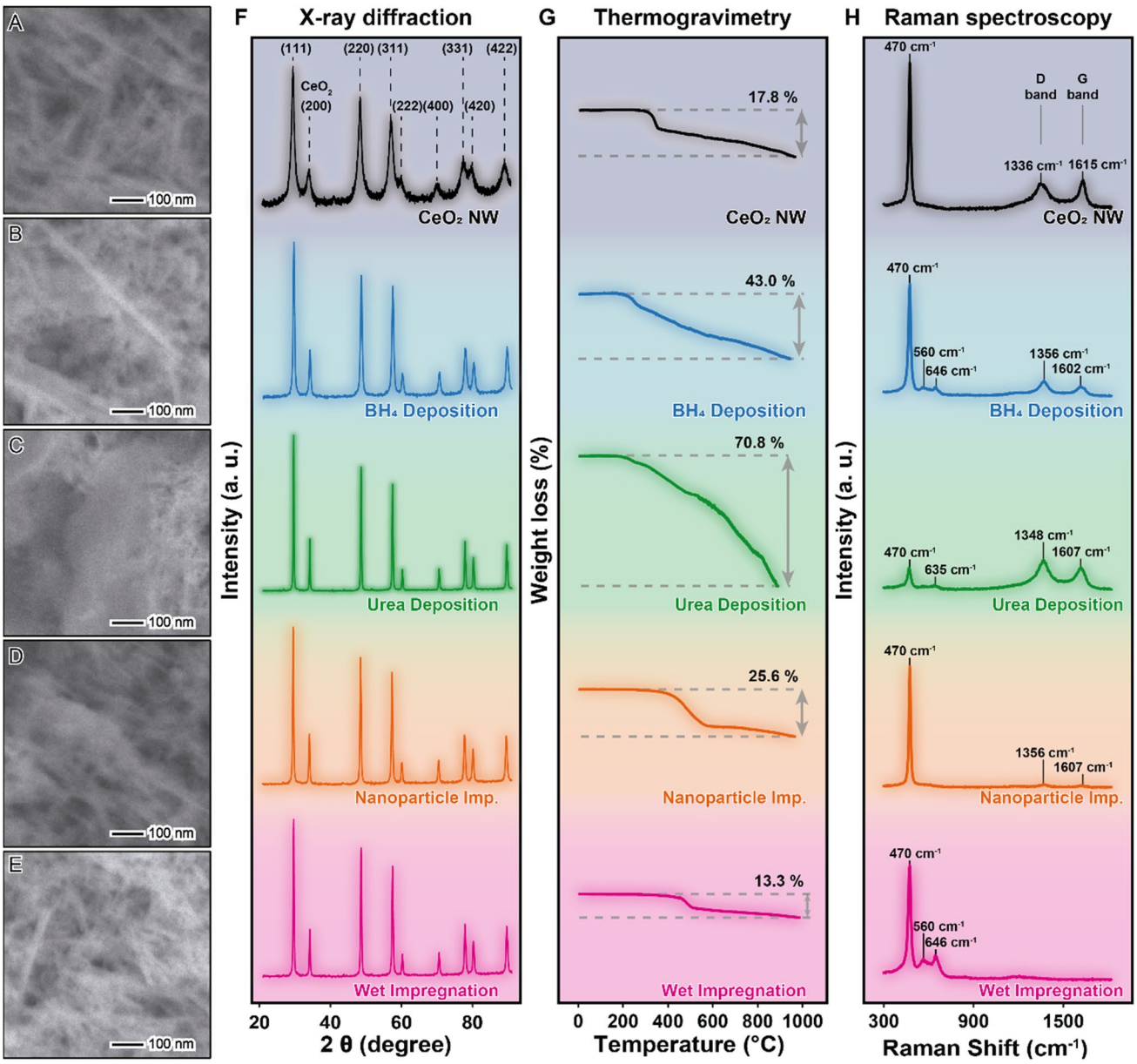

Fig. 7 SEM images of the CeO_2 nanowires (**A**), Ni/CeO_2 wet impregnation (**B**), nanoparticles impregnation (**C**), urea deposition (**D**), and BH_4 deposition (**E**), along with XRD spectra (**F**), TGA profile (**G**), and Raman spectra (**H**) for Ni/CeO_2 synthesized using different methods and CeO_2 nanowires after the catalytic experiment

after the catalytic experiments. These data demonstrate the robustness of CeO_2 nanowires. TGA (Fig. 7G) depicts the investigation for the formation of solid carbon-based structures. Raman analyses (Fig. 7H) present the deposition of solid carbon-based materials with different structures over the catalysts. Ethanol steam reforming can also produce carbon structures through reactions such as the decomposition of methane (Eq. 27), ethene (Eq. 28), acetaldehyde (Eq. 29), and acetone (Eq. 30) [126, 134].

$$CH_{4(ads)} \rightarrow C_{(s)} + 2H_{2(g)} \tag{27}$$

$$C_2H_{4(ads)} \rightarrow 2\ C_{(s)} + 2H_{2(g)} \tag{28}$$

$$C_3CHO_{(ads)} \rightarrow 4\ C_{(s)} \tag{29}$$

$$CH_3(CO)CH_{3(ads)} \rightarrow C_{(s)} \quad (30)$$

The CeO_2 nanowires show a small amount of carbon mass on the surface, with mass loss exhibiting a narrow main event around 350 °C and progressive loss until 1,000 °C. The Raman spectra indicate well-crystallized carbon deposition with an I_D/I_G ratio of 0.9. This corroborates the catalytic experiment, suggesting that the CeO_2 nanowires remained active for the entire 48 h, and XPS analysis indicates that oxygen vacancies are crucial in preventing excessive carbon deposition and deactivation. Furthermore, an efficient synthesis method to incorporate an active metal on the support surface can enhance catalytic activity and surface reactivity to be more stable. This is evident in the Ni/CeO_2 wet impregnation method, which shows a clear catalyst surface with minimal carbon deposition, lower mass loss compared to CeO_2 nanowires, and no detection of the D and G bands in the Raman spectra. TGA analysis reveals that Ni/CeO_2 wet impregnation exhibits the lowest mass loss (13.3%) with a well-defined event at 500 °C, and SEM images confirm the absence of a considerable amount of solid carbon on the surfaces of the nanowires in the Ni/CeO_2 wet impregnation sample.

In sequence, the effect of size and metal-support interaction may contribute to carbon deposition. Comparatively, the Ni/CeO_2 wet impregnation is characterized by a thin layer and weak metal-support interaction, contributing to low carbon deposition. This can be attributed to the thin layer promoting homogeneous active sites, as observed in H_2-TPD, and providing support to prevent carbon deposition [27, 122]. However, modifying the structure to spherical Ni nanoparticles with a size of 5 nm and weak metal-support interaction, the Ni/CeO_2 nanoparticles impregnation exhibited higher catalytic deactivation due to increased carbon deposition (Fig. 7B) and a mass loss of 25.6%. Incrasing particle size and enhancing metal-support interaction, the Ni/CeO_2 urea deposition formed agglomerated nanoparticles around 15 nm with very strong metal-support interaction, resulting in a significant amount of carbon deposition. Figure 7C displays a thick carbon mass layer covering the Ni/CeO_2 urea deposition and the most pronounced mass loss among the catalysts. This explains the highest deactivation observed within the first 24 h of the catalytic experiment. It may be associated with the previous supposition that high energetic sites are titrated by chemisorbed reactants and products, as evidenced by H_2-TPD where H_2 was desorbed at a higher temperature. Additionally, a lower metal-support interaction in the Ni/CeO_2 BH_4 deposition results in intermediate carbon deposition with carbon spots on the catalyst (Fig. 7D) and 43.0% mass oss. The Raman spectra show similar carbon structures for Ni/CeO_2 nanoparticles impregnation (I_D/I_G = 1.5), urea deposition (I_D/I_G = 1.4), and BH_4 deposition (I_D/I_G = 1.5). This demonstrates the influence of the incorporation synthesis methods of the active phase on changing the surface reactivity of the catalysts.

4 Conclusions

In summary, our results demonstrate the synthesis of Ni/CeO_2 using four different methods: (i) wet impregnation, (ii) nanoparticles impregnation, (iii) urea deposition, and (iv) BH_4 deposition, resulting in well-defined shapes, sizes, and compositions, all showing high performance in ethanol steam reforming. These synthesis methods produced four distinct nanostructures and particle sizes for nickel: (i) a thin layer on the CeO_2 nanowires, (ii) small nanoparticles of 5 nm, (iii) agglomerated nanoparticles of 15 nm, and (iv) large nanoparticles of 35 nm. In conclusion, three synthesis methods—wet impregnation, nanoparticles impregnation, and BH_4 deposition—yielded catalysts with controlled characteristics and properties after heating at 450 °C under H_2 atmosphere, while urea deposition showed agglomeration. In terms of catalytic performance, all Ni/CeO_2 catalysts exhibited 100% ethanol conversion throughout the catalytic experiment and high (~ 70%) H_2 selectivity under high contact time conditions: wet impregnation (68.8%), BH4 deposition (67.6%), nanoparticles impregnation (66.6%), urea deposition (65.2%), and CeO_2 nanowires (9.9%). The obtained catalysts were relatively similar in composition and catalytic activity but differed in synthesis methods. However, in low contact time experiments, the Ni/CeO_2 catalysts displayed differentiated surface reactivity. Specifically, catalytic properties depended on physicochemical properties such as nanoparticle size, metal dispersion, metal-support interaction, and synthesis methods. In terms of stability, impregnation methods exhibited high stability, with ethanol conversion rates above 78% and 60% for wet impregnation and nanoparticles impregnation, respectively, after 48 h of catalytic experiment. However, BH_4 deposition exhibited intermediate stability, with an ethanol conversion rate around 37% after 48 h, while urea deposition showed strong deactivation of 86% after the test. In terms of H_2 yield and stability, the Ni/CeO_2 wet impregnation method was the most effective catalyst, showing a high H_2 yield close to the theoretical maximum and lower deactivation. The average H_2 yield for each catalyst was: wet impregnation (66%), BH_4 deposition (65%), nanoparticles impregnation (54%), urea deposition (22%), and CeO_2 nanowire (7%). Considering experimental error, wet impregnation, nanoparticles impregnation, and BH_4 deposition yielded similar H_2 yields. These results suggest that the choice of synthesis method for heterogeneous nanocatalysts is crucial for preparing nanomaterials with exceptional catalytic performance. We believe that our findings make a significant contribution to the synthesis of

supported catalysts for gas-phase transformations, such as ethanol steam reforming.

Supplementary Information The online version contains supplementary material available at https://doi.org/10.1007/s42247-024-00793-z.

Acknowledgements We are grateful to the Fundação de Amparo à Pesquisa do Estado do Rio de Janeiro (FAPERJ), grant numbers E-26/201.431/2021 and E-26/211.612/2019; to the Conselho Nacional de Desenvolvimento Científico e Tecnológico—CNPq, grant number 317288/2021-0; and to the Coordenação de Aperfeiçoamento de Pessoal de Nível Superior—Brasil (CAPES)—Finance Code 001, grant number 88887.645934/2021-00. We thanks to CEM (Central Experimental Multiusuário) of the Federal University of ABC (UFABC). We thanks to Institute of Chemistry (IQ) at University of São Paulo for the analysis facilities.

Declarations

Competing interests The authors declare no competing interests.

References

1. P. Suchomel, L. Kvitek, R. Prucek, A. Panacek, A. Halder, S. Vajda, R. Zboril, Simple size-controlled synthesis of au nanoparticles and their size-dependent Catalytic activity. Sci. Rep. **8**, 4589 (2018). https://doi.org/10.1038/s41598-018-22976-5
2. A. Trovarelli, J. Llorca, Ceria catalysts at Nanoscale: how do Crystal shapes shape catalysis? ACS Catal. **7**, 4716–4735 (2017). https://doi.org/10.1021/acscatal.7b01246
3. P.H.C. Camargo, T.S. Rodrigues, da A.G.M. Silva, J. Wang, Controlled synthesis: nucleation and growth in solution. *Metallic Nanostructures*; Springer International Publishing: Cham, 2015; 49–74
4. Z. Kou, X. Li, L. Zhang, W. Zang, X. Gao, J. Wang, Dynamic Surface Chemistry of catalysts in Oxygen Evolution reaction. Small Sci. **1**, 2100011 (2021). https://doi.org/10.1002/smsc.202100011
5. de P. Souza, L. Silvester, da A. Silva, C. Fernandes, T. Rodrigues, S. Paul, P. Camargo, R. Wojcieszak, Exploiting the Synergetic Behavior of PtPd Bimetallic catalysts in the selective hydrogenation of glucose and Furfural. Catalysts. **9**, 132 (2019). https://doi.org/10.3390/catal9020132
6. Y. Lou, J. Xu, Y. Zhang, C. Pan, Y. Dong, Y. Zhu, Metal-Support Interaction for Heterogeneous Catalysis: from nanoparticles to single atoms. Mater. Today Nano. **12**, 100093 (2020). https://doi.org/10.1016/j.mtnano.2020.100093
7. C.-J. Pan, M.-C. Tsai, W.-N. Su, J. Rick, N.G. Akalework, A.K. Agegnehu, S.-Y. Cheng, B.-J. Hwang, Tuning/Exploiting strong Metal-Support Interaction (SMSI) in heterogeneous catalysis. J. Taiwan. Inst. Chem. Eng. **74**, 154–186 (2017). https://doi.org/10.1016/j.jtice.2017.02.012
8. R.A. El-Salamony, Catalytic steam reforming of ethanol to produce hydrogen: modern and efficient catalyst modification strategies. ChemistrySelect **8** (2023). https://doi.org/10.1002/slct.202203195
9. R.S. Geonmonond, A.G.M. da Silva, T.S. Rodrigues, I.C. de Freitas, R.A. Ando, T.V. Alves, P.H.C. Camargo, Addressing the effects of size-dependent absorption, scattering, and near-field enhancements in plasmonic catalysis. ChemCatChem **10**, 3447–3452 (2018). https://doi.org/10.1002/cctc.201800691
10. C.M. Kisukuri, D.J. Palmeira, T.S. Rodrigues, P.H.C. Camargo, L.H. Andrade, Bimetallic nanoshells as platforms for metallo- and biometallo-catalytic applications. ChemCatChem **8**, 171–179 (2016). https://doi.org/10.1002/cctc.201500812
11. Y. Xin, K. Yu, L. Zhang, Y. Yang, H. Yuan, H. Li, L. Wang, J. Zeng, Copper-based Plasmonic Catalysis: recent advances and future perspectives. Adv. Mater. **33**, 2008145 (2021). https://doi.org/10.1002/adma.202008145
12. R. Suresh, V. Ponnuswamy, R. Mariappan, Effect of Annealing temperature on the Microstructural, Optical and Electrical properties of CeO2 nanoparticles by Chemical Precipitation Method. Appl. Surf. Sci. **273**, 457–464 (2013). https://doi.org/10.1016/j.apsusc.2013.02.062
13. T. Alammar, H. Noei, Y. Wang, W. Grünert, A.-V. Mudring, Ionic liquid-assisted Sonochemical Preparation of CeO 2 nanoparticles for CO oxidation. ACS Sustain. Chem. Eng. **3**, 42–54 (2015). https://doi.org/10.1021/sc500387k
14. R.-J. Qi, Y.-J. Zhu, G.-F. Cheng, Y.-H. Huang, Sonochemical synthesis of single-crystalline CeOHCO 3 rods and their Thermal Conversion to CeO 2 rods. Nanotechnology. **16**, 2502–2506 (2005). https://doi.org/10.1088/0957-4484/16/11/006
15. N.S. Ferreira, R.S. Angélica, V.B. Marques, de C.C.O. Lima, M.S. Silva, Cassava-Starch-assisted Sol–Gel synthesis of CeO 2 nanoparticles. Mater. Lett. **165**, 139–142 (2016). https://doi.org/10.1016/j.matlet.2015.11.107
16. J. Gong, F. Meng, X. Yang, Z. Fan, H. Li, Controlled hydrothermal synthesis of triangular CeO2 nanosheets and their formation mechanism and Optical properties. J. Alloys Compd. **689**, 606–616 (2016). https://doi.org/10.1016/j.jallcom.2016.08.030
17. D. Xue, Y. Wang, J. Cao, Z. Zhang, Hydrothermal synthesis of CeO2-SnO2 nanoflowers for improving triethylamine gas sensing property. Nanomaterials **8**, 1025 (2019). https://doi.org/10.3390/nano8121025
18. T.S. Rodrigues, de A.B.L. Moura, F.A. e Silva, E.G. Candido, da A.G.M. Silva, de D.C. Oliveira, J. Quiroz, P.H.C. Camargo, V.S. Bergamaschi, J.C. Ferreira et al., Ni supported Ce0.9Sm0.1O2-δ nanowires: an efficient catalyst for ethanol steam reforming for hydrogen production. Fuel **237**, 1244–1253 (2019). https://doi.org/10.1016/j.fuel.2018.10.053
19. da A.G.M. Silva, D.C. Batalha, T.S. Rodrigues, E.G. Candido, S.C. Luz, de I.C. Freitas, F.C. Fonseca, de D.C. Oliveira, J.G. Taylor, de S.I.C. Torresi et al., Sub-15 nm CeO 2 nanowires as an efficient Non-noble Metal Catalyst in the room-temperature oxidation of Aniline. Catal. Sci. Technol. **8**, 1828–1839 (2018). https://doi.org/10.1039/C7CY02402A
20. H. Meng, J. Zhang, Y. Yang, Recent status in catalyst modification strategies for hydrogen production from ethanol steam reforming. ChemCatChem **15** (2023). https://doi.org/10.1002/cctc.202300733
21. I.I. Soykal, H. Sohn, U.S. Ozkan, Effect of support particle size in Steam Reforming of Ethanol over Co/CeO $_2$ catalysts. ACS Catal. **2**, 2335–2348 (2012). https://doi.org/10.1021/cs3004159
22. I.I. Soykal, H. Sohn, D. Singh, J.T. Miller, U.S. Ozkan, Reduction characteristics of Ceria under ethanol steam reforming conditions: Effect of the particle size. ACS Catal. **4**, 585–592 (2014). https://doi.org/10.1021/cs400908h
23. M. Jaramillo-Baquero, J. Múnera, L. Cornaglia, Ethylene glycol-modified CeO2-SiO2 support for Co catalysts Applied in the ethanol steam reforming. Fuel. **367**, 131473 (2024). https://doi.org/10.1016/j.fuel.2024.131473
24. N. Wang, Y. Feng, Y. Chen, X. Guo, Lithium-based Sorbent from Rice Husk materials for Hydrogen Production via Sorption-enhanced steam reforming of ethanol. Fuel. **245**, 263–273 (2019). https://doi.org/10.1016/j.fuel.2019.02.048
25. A. Ashar, M. Iqbal, I.A. Bhatti, M.Z. Ahmad, K. Qureshi, J. Nisar, I.H. Bukhari, Synthesis, Characterization and

photocatalytic activity of ZnO Flower and Pseudo-sphere: Nonylphenol Ethoxylate degradation under UV and solar irradiation. J. Alloys Compd. **678**, 126–136 (2016). https://doi.org/10.1016/j.jallcom.2016.03.251
26. S.B. Kashid, R.W. Raut, Y.S. Malghe, Microwave assisted synthesis of Nickel nanostructures by Hydrazine Reduction Route: Effect of Solvent and Capping Agent on morphology and magnetic properties. Mater. Chem. Phys. **170**, 24–31 (2016). https://doi.org/10.1016/j.matchemphys.2015.12.014
27. M.-R. Li, Y.-Y. Song, G.-C. Wang, The Mechanism of Steam-Ethanol Reforming on Co_{13}/CeO_{2-x}: A DFT Study. ACS Catal. **9**, 2355–2367 (2019). https://doi.org/10.1021/acscatal.8b03765
28. e F. Silva, V. Salim, T. Rodrigues, Controlled nickel nanoparticles: a review on how parameters of synthesis can modulate their features and properties. AppliedChem **4**, 86–106 (2024). https://doi.org/10.3390/appliedchem4010007
29. e F.A. Silva, T.S. Rodrigues, Recent advances in the Use of Controlled nanocatalysts in Methane Conversion reactions. Methane. **3**, 359–379 (2024). https://doi.org/10.3390/methane3020020
30. J. Vecchietti, P. Pérez-Bailac, P.G. Lustemberg, E.L. Fornero, L. Pascual, M.V. Bosco, A. Martínez-Arias, M.V. Ganduglia-Pirovano, A.L. Bonivardi, Shape-controlled pathways in the Hydrogen production from ethanol steam reforming over Ceria Nanoparticles. ACS Catal. **12**, 10482–10498 (2022). https://doi.org/10.1021/acscatal.2c02117
31. M. Wang, S.Y. Kim, A. Jamsaz, N. Pham-Ngoc, Y. Men, D.H. Jeong, E.W. Shin, Metal–support interactions over Ni/CeO2–ZrO2 catalysts for ethanol steam reforming and their effects on the Coke Gasification. Catal. Today. **425**, 114341 (2024). https://doi.org/10.1016/j.cattod.2023.114341
32. K. Mukai, Interfacial, Phenomena, Metals Processing and Properties. *Fundamentals of Metallurgy*; Elsevier, 2005; 237–269
33. N.T.K. Thanh, N. Maclean, S. Mahiddine, Mechanisms of Nucleation and Growth of nanoparticles in Solution. Chem. Rev. **114**, 7610–7630 (2014). https://doi.org/10.1021/cr400544s
34. A. Nur, W. Mazli, M. Afnan Ahmad, S. Samsuri, Nucleation. *Synthesis Methods and Crystallization*; IntechOpen, 2020
35. INTRODUCTION. In, *Handbook of Nucleating Agents* (Elsevier, 2016), pp. 1–3
36. M.J. Ndolomingo, N. Bingwa, R. Meijboom, Review of supported metal nanoparticles: synthesis methodologies, advantages and application as catalysts. J. Mater. Sci. **55**, 6195–6241 (2020). https://doi.org/10.1007/s10853-020-04415-x
37. X. Liu, X. Liang, N. Zhang, G. Qiu, R. Yi, Selective synthesis and characterization of Sea Urchin-like metallic nickel nanocrystals. Mater. Sci. Engineering: B **132**, 272–277 (2006). https://doi.org/10.1016/j.mseb.2006.04.024
38. X. Ni, Q. Zhao, D. Zhang, X. Zhang, H. Zheng, Novel hierarchical nanostructures of Nickel: self-assembly of Hexagonal Nanoplatelets. J. Phys. Chem. C **111**, 601–605 (2007). https://doi.org/10.1021/jp065832j
39. da A.G.M. Silva, T.S. Rodrigues, E.G. Candido, de I.C. Freitas, da A.H.M. Silva, H.V. Fajardo, R. Balzer, J.F. Gomes, J.M. Assaf, de D.C. Oliveira et al., Combining active phase and support optimization in MnO2-Au Nanoflowers: enabling high activities towards Green oxidations. J. Colloid Interface Sci. **530**, 282–291 (2018). https://doi.org/10.1016/j.jcis.2018.06.089
40. J. Guan, L. Liu, L. Xu, Z. Sun, Y. Zhang, Nickel flower-like nanostructures composed of nanoplates: one-pot synthesis, stepwise growth mechanism and enhanced ferromagnetic properties. CrystEngComm **13**, 2636 (2011). https://doi.org/10.1039/c0ce00805b
41. A.G.M. da Silva, M.L. de Souza, T.S. Rodrigues, R.S. Alves, M.L.A. Temperini, P.H.C. Camargo, da A.G.M. Silva, de M.L. Souza, T.S. Rodrigues, R.S. Alves et al., Rapid Synthesis of Hollow Ag-Au nanodendrites in 15 seconds by combining galvanic replacement and precursor reduction reactions. Chem.---Eur. J. **20**, 15040–15046 (2014). https://doi.org/10.1002/chem.201404739
42. da A.H.M. Silva, T.S. Rodrigues, da A.G.M. Silva, P.H.C. Camargo, J.F. Gomes, J.M. Assaf, Systematic investigation of the Effect of Oxygen mobility on CO Oxidation over AgPt nanoshells supported on CeO2, TiO2 and Al2O3. J. Mater. Sci. **52**, 13764–13778 (2017). https://doi.org/10.1007/s10853-017-1481-z
43. T.S. Rodrigues, A.G.M. da Silva, M.C. Gonçalves, H.V. Fajardo, R. Balzer, L.F.D. Probst, P.H.C. Camargo, AgPt hollow nanodendrites: synthesis and uniform dispersion over SiO_2 support for catalytic applications. ChemNanoMat **1**, 46–51 (2015). https://doi.org/10.1002/cnma.201500025
44. J. Quinson, M. Inaba, S. Neumann, A.A. Swane, J. Bucher, S.B. Simonsen, L. Theil Kuhn, J.J.K. Kirkensgaard, K.M.Ø. Jensen, M. Oezaslan et al., Investigating particle size effects in Catalysis by applying a size-controlled and surfactant-free synthesis of Colloidal nanoparticles in Alkaline Ethylene Glycol: Case Study of the Oxygen reduction reaction on pt. ACS Catal. **8**, 6627–6635 (2018). https://doi.org/10.1021/acscatal.8b00694
45. F. Gorky, A. Best, J. Jasinski, B.J. Allen, A.C. Alba-Rubio, M.L. Carreon, Plasma Catalytic Ammonia Synthesis on Ni nanoparticles: the size effect. J. Catal. **393**, 369–380 (2021). https://doi.org/10.1016/j.jcat.2020.11.030
46. Y. Shi, J. Wang, R. Zhou, Pt-Support Interaction and nanoparticle size effect in Pt/CeO2–TiO2 catalysts for low temperature VOCs removal. Chemosphere. **265**, 129127 (2021). https://doi.org/10.1016/j.chemosphere.2020.129127
47. L. Macheli, E. Carleschi, B.P. Doyle, G. Leteba, van E. Steen, Tuning Catalytic Performance in Fischer-Tropsch synthesis by metal-support interactions. J. Catal. **395**, 70–79 (2021). https://doi.org/10.1016/j.jcat.2020.12.023
48. K. Ament, D.R. Wagner, T. Götsch, T. Kikuchi, J. Kröhnert, A. Trunschke, T. Lunkenbein, T. Sasaki, J. Breu, Enhancing the Catalytic activity of Palladium nanoparticles via Sandwich-Like Confinement by Thin Titanate Nanosheets. ACS Catal. **11**, 2754–2762 (2021). https://doi.org/10.1021/acscatal.1c00031
49. T.S. Rodrigues, M. Zhao, T. Yang, K.D. Gilroy, da A.G.M. Silva, P.H.C. Camargo, Y. Xia, Synthesis of Colloidal Metal Nanocrystals: a Comprehensive Review on the reductants. Chem. – Eur. J. **24**, 16944–16963 (2018). https://doi.org/10.1002/chem.201802194
50. Z.R. Parekh, S.H. Chaki, A.B. Hirpara, G.H. Patel, R.M. Kannaujiya, A.J. Khimani, M.P. Deshpande, CuO nanoparticles – synthesis by wet precipitation technique and its characterization. Phys. B Condens. Matter. **610**, 412950 (2021). https://doi.org/10.1016/j.physb.2021.412950
51. K. Yan, F. Xu, W. Wei, C. Yang, D. Wang, X. Shi, Electrochemical synthesis of Chitosan/Silver Nanoparticles Multilayer Hydrogel Coating with PH-Dependent Controlled Release Capability and Antibacterial Property. Colloids Surf. B Biointerfaces. **202**, 111711 (2021). https://doi.org/10.1016/j.colsurfb.2021.111711
52. P. Zhang, H. Liu, X. Li, Photo-reduction synthesis of Cu nanoparticles as Plasmon-Driven Non-semiconductor Photocatalyst for overall water splitting. Appl. Surf. Sci. **535**, 147720 (2021). https://doi.org/10.1016/j.apsusc.2020.147720
53. K. Murugesan, M. Beller, R.V. Jagadeesh, Reusable nickel nanoparticles-catalyzed reductive amination for selective synthesis of primary amines. Angew. Chem. **131**, 5118–5122 (2019). https://doi.org/10.1002/ange.201812100
54. J. Yang, Z. Qiu, C. Zhao, W. Wei, W. Chen, Z. Li, Y. Qu, J. Dong, J. Luo, Z. Li et al., In situ thermal atomization to convert supported Nickel nanoparticles into surface-bound Nickel single-atom catalysts. Angew. Chem. Int. Ed. **57**, 14095–14100 (2018). https://doi.org/10.1002/anie.201808049

55. K. Guo, H. Li, Z. Yu, Size-dependent Catalytic activity of Monodispersed Nickel nanoparticles for the Hydrolytic Dehydrogenation of Ammonia Borane. ACS Appl. Mater. Interfaces. **10**, 517–525 (2018). https://doi.org/10.1021/acsami.7b14166
56. A. Desgagnés, O. Alizadeh Sahraei, M.C. Iliuta, Improvement strategies for Ni-Based Alcohol Steam reforming catalysts. J. Energy Chem. **86**, 447–479 (2023). https://doi.org/10.1016/j.jechem.2023.07.011
57. V. Aker, N. Ayas, Boosting hydrogen production by ethanol steam reforming on Cobalt-modified Ni–Al2O3 Catalyst. Int. J. Hydrogen Energy. **48**, 22875–22888 (2023). https://doi.org/10.1016/j.ijhydene.2022.12.310
58. H. Alipour, S.M. Alavi, M. Rezaei, E. Akbari, M. Varbar, The role of various Preparation techniques and nickel loadings in ethanol steam reforming over Mesoporous Nanostructured Ni–Al2O3 catalysts. J. Energy Inst. **112**, 101488 (2024). https://doi.org/10.1016/j.joei.2023.101488
59. da A.L.M. Silva, den J.P. Breejen, L.V. Mattos, J.H. Bitter, de K.P. Jong, F.B. Noronha, Cobalt particle size effects on Catalytic performance for ethanol steam reforming – smaller is better. J. Catal. **318**, 67–74 (2014). https://doi.org/10.1016/j.jcat.2014.07.020
60. G.C. Bond, The origins of particle size effects in Heterogeneous Catalysis. Surf. Sci. **156**, 966–981 (1985). https://doi.org/10.1016/0039-6028(85)90273-0
61. A. Hernando, P. Crespo, M.A. García, Metallic magnetic nanoparticles. Sci. World J. **5**, 972–1001 (2005). https://doi.org/10.1100/tsw.2005.121
62. M. Rangel de Melo Rodrigues, R. Machado Ferreira, dos F. Santos Pereira, F. Anchieta e Silva, A. César Azevedo Silva, H. Aguilar Vitorino, de Jesus Gomes Varela Júnior, J. Atsushi Tanaka, A. Aurélio, M. Suller Garcia, Silva Rodrigues, T. Application of AgPt nanoshells in direct methanol fuel cells: experimental and theoretical insights of design electrocatalysts over methanol crossover effect. ChemCatChem **14** (2022). https://doi.org/10.1002/cctc.202200605
63. C. Wang, X. Ren, C. Chen, H. Cao, Effect of Calcination Temperature on Co/Sepiolite Catalyst for Hydrogen Production by Ethanol Steam Reforming: Co speciation from Phyllosilicate to Spinel. Chem. Eng. Res. Des. **203**, 595–607 (2024). https://doi.org/10.1016/j.cherd.2024.01.043
64. H. Meng, Y. Yang, T. Shen, W. Liu, L. Wang, P. Yin, Z. Ren, Y. Niu, B. Zhang, L. Zheng et al., A strong Bimetal-Support Interaction in ethanol steam reforming. Nat. Commun. **14**, 3189 (2023). https://doi.org/10.1038/s41467-023-38883-x
65. M. Wang, S.Y. Kim, A. Jamsaz, N. Pham-Ngoc, Y. Men, D.H. Jeong, E.W. Shin, Effect of active sites distributions on temperature dependent–coke formation over Ni/CexZr1 – xO2–Al2O3 catalysts for ethanol steam reforming: Coke Precursor Gasification. Appl. Surf. Sci. **644**, 158746 (2024). https://doi.org/10.1016/j.apsusc.2023.158746
66. C. Quan, Z. Gao, X. Liu, N. Miskolczi, Ethanol Steam Reforming for Hydrogen Production under Ni/Ce catalysts. J. Energy Inst. **112**, 101446 (2024). https://doi.org/10.1016/j.joei.2023.101446
67. T.S. Rodrigues, F.A. e Silva, E.G. Candido, da A.G.M. Silva, S. Geonmonond, R. Camargo, P.H.C. Linardi, M. Fonseca, F.C. Ethanol steam reforming: understanding changes in the activity and stability of Rh/MxOy catalysts as function of the support. J Mater Sci **54**, 11400–11416 (2019). https://doi.org/10.1007/s10853-019-03660-z
68. C.-K. Tsung, X. Kou, Q. Shi, J. Zhang, M.H. Yeung, J. Wang, G.D. Stucky, Selective shortening of single-crystalline gold nanorods by mild oxidation. J. Am. Chem. Soc. **128**, 5352–5353 (2006). https://doi.org/10.1021/ja060447t
69. da A.H. Silva, C.M. Kisukuri, T.S. Rodrigues, E.G. Candido, de I.C. Freitas, da A.H. Silva, J.M. Assaf, D.C. Oliveira, L.H. Andrade, P.H.C. Camargo, MnO2 nanowires decorated with au Ultrasmall nanoparticles for the Green Oxidation of Silanes and Hydrogen Production under Ultralow Loadings. Appl. Catal. B **184**, 35–43 (2016). https://doi.org/10.1016/j.apcatb.2015.11.023
70. C. Huck-Iriart, L. Soler, A. Casanovas, C. Marini, J. Prat, J. Llorca, C. Escudero, Unraveling the Chemical State of Cobalt in Co-based catalysts during ethanol steam reforming: an in situ study by Near ambient pressure XPS and XANES. ACS Catal. **8**, 9625–9636 (2018). https://doi.org/10.1021/acscatal.8b02666
71. K. Cheng, W. Song, Y. Cheng, J. Liu, Z. Zhao, Y. Wei, Selective Catalytic reduction over Size-Tunable Rutile TiO 2 Nanorod Microsphere-supported CeO 2 catalysts. Catal. Sci. Technol. **6**, 4478–4490 (2016). https://doi.org/10.1039/C5CY02121A
72. X. Zhang, F. Hou, Y. Yang, Y. Wang, N. Liu, D. Chen, Y. Yang, A facile synthesis for cauliflower like CeO2 catalysts from Ce-BTC Precursor and their Catalytic Performance for CO Oxidation. Appl. Surf. Sci. **423**, 771–779 (2017). https://doi.org/10.1016/j.apsusc.2017.06.235
73. M. Yin, W. Qiu, L. Song, H. Zhu, Y. Chen, S. Li, J. Cheng, Y. Sun, G. Bai, G. Zhang et al., Promoting effect of organic ligand on the performance of ceria for the selective catalytic reduction of NO by NH 3. ChemistrySelect **3**, 2683–2691 (2018). https://doi.org/10.1002/slct.201800088
74. X. Yan, T. Hu, P. Liu, S. Li, B. Zhao, Q. Zhang, W. Jiao, S. Chen, P. Wang, J. Lu et al., Highly efficient and stable Ni/CeO2-SiO2 Catalyst for Dry Reforming of methane: Effect of Interfacial structure of Ni/CeO2 on SiO2. Appl. Catal. B **246**, 221–231 (2019). https://doi.org/10.1016/j.apcatb.2019.01.070
75. R.J.O. Mossanek, I. Preda, M. Abbate, J. Rubio-Zuazo, G.R. Castro, A. Vollmer, A. Gutiérrez, L. Soriano, Investigation of Surface and Non-local Screening effects in the Ni 2p Core Level Photoemission Spectra of NiO. Chem. Phys. Lett. **501**, 437–441 (2011). https://doi.org/10.1016/j.cplett.2010.11.050
76. L. Soriano, I. Preda, A. Gutiérrez, S. Palacín, M. Abbate, A. Vollmer, Surface Effects in the Ni 2*p* x-rayp x-ray photoemission spectra of NiO. Phys Rev B **75**, 233417 (2007). https://doi.org/10.1103/PhysRevB.75.233417.
77. I. Preda, R.J.O. Mossanek, M. Abbate, L. Alvarez, J. Méndez, A. Gutiérrez, L. Soriano, Surface contributions to the XPS Spectra of Nanostructured NiO deposited on HOPG. Surf. Sci. **606**, 1426–1430 (2012). https://doi.org/10.1016/j.susc.2012.05.005
78. S. Oswald, W.X.P.S. Brückner, Depth Profile Analysis of Non-stoichiometric NiO films. Surf. Interface Anal. **36**, 17–22 (2004). https://doi.org/10.1002/sia.1640
79. M.A. Peck, M.A. Langell, Comparison of Nanoscaled and Bulk NiO Structural and Environmental characteristics by XRD, XAFS, and XPS. Chem. Mater. **24**, 4483–4490 (2012). https://doi.org/10.1021/cm300739y
80. C. Cerdá-Moreno, J.F. Costa-Serra, A. Da; Chica, Co and La supported on Zn-Hydrotalcite-derived material as efficient Catalyst for ethanol steam reforming. Int. J. Hydrogen Energy. **44**, 12685–12692 (2019). https://doi.org/10.1016/j.ijhydene.2019.01.156
81. T. Ohno, S. Ochibe, H. Wachi, S. Hirai, T. Arai, N. Sakamoto, H. Suzuki, T. Matsuda, Preparation of Metal Catalyst Component Doped Perovskite Catalyst particle for Steam reforming process by Chemical Solution Deposition with partial reduction. Adv. Powder Technol. **29**, 584–589 (2018). https://doi.org/10.1016/j.apt.2017.11.030
82. J.A. Konvalinka, P.H. Oeffelt, J.J.F. Van; Scholten, Temperature programmed Desorption of Hydrogen from Nickel catalysts. Appl. Catal. **1**, 141–158 (1981). https://doi.org/10.1016/0166-9834(81)80002-4
83. H. Du, Y. Wang, H. Arandiyan, A. Younis, J. Scott, B. Qu, T. Wan, X. Lin, J. Chen, D. Chu, Design and synthesis of CeO2 Nanowire/MnO2 Nanosheet Heterogeneous structure for

enhanced Catalytic properties. Mater. Today Commun. **11**, 103–111 (2017). https://doi.org/10.1016/j.mtcomm.2017.03.002
84. Y. Ji, X.A. Liu, Nanoporous, CeO 2 nanowire array by Acid Etching Preparation: an efficient Electrocatalyst for ambient N 2 reduction. Mater. Adv. **2**, 3552–3555 (2021). https://doi.org/10.1039/D1MA00243K
85. X. Ma, P. Lu, P. Wu, Structural, Optical and magnetic properties of CeO2 nanowires with nonmagnetic Mg2 + doping. J. Alloys Compd. **734**, 22–28 (2018). https://doi.org/10.1016/j.jallcom.2017.11.023
86. R. Zanella, L. Delannoy, C. Louis, Mechanism of deposition of gold precursors onto TiO2 during the Preparation by Cation Adsorption and deposition–precipitation with NaOH and urea. Appl. Catal. Gen. **291**, 62–72 (2005). https://doi.org/10.1016/j.apcata.2005.02.045
87. G.G. Couto, J.J. Klein, W.H. Schreiner, D.H. Mosca, de A.J.A. Oliveira, A.J.G. Zarbin, Nickel nanoparticles obtained by a modified polyol process: synthesis, characterization, and magnetic properties. J. Colloid Interface Sci. **311**, 461–468 (2007). https://doi.org/10.1016/j.jcis.2007.03.045
88. G. Mattei, P. Mazzoldi, M.L. Post, D. Buso, M. Guglielmi, A. Martucci, Cookie-like Au/NiO nanoparticles with Optical Gas-Sensing properties. Adv. Mater. **19**, 561–564 (2007). https://doi.org/10.1002/adma.200600930
89. F.T. Thema, E. Manikandan, A. Gurib-Fakim, M. Maaza, Single phase Bunsenite NiO nanoparticles Green synthesis by Agathosma Betulina Natural Extract. J. Alloys Compd. **657**, 655–661 (2016). https://doi.org/10.1016/j.jallcom.2015.09.227
90. M. Patange, S. Biswas, A.K. Yadav, S.N. Jha, D. Bhattacharyya, Morphology-controlled synthesis of Monodispersed Graphitic Carbon Coated Core/Shell Structured Ni/NiO Nanoparticles with enhanced Magnetoresistance. Phys. Chem. Chem. Phys. **17**, 32398–32412 (2015). https://doi.org/10.1039/C5CP05830A
91. K. Karthik, M. Shashank, V. Revathi, T. Tatarchuk, Facile microwave-assisted green synthesis of NiO nanoparticles from Andrographis Paniculata Leaf Extract and evaluation of their photocatalytic and anticancer activities. Mol. Cryst. Liq. Cryst. **673**, 70–80 (2018). https://doi.org/10.1080/15421406.2019.1578495
92. P.X. Huang, F. Wu, B.L. Zhu, X.P. Gao, H.Y. Zhu, T.Y. Yan, W.P. Huang, S.H. Wu, D.Y. Song, CeO 2 nanorods and gold nanocrystals supported on CeO 2 nanorods as Catalyst. J. Phys. Chem. B **109**, 19169–19174 (2005). https://doi.org/10.1021/jp052978u
93. J. Védrine, Heterogeneous catalysis on metal oxides. Catalysts. **7**, 341 (2017). https://doi.org/10.3390/catal7110341
94. P. Li, X. Chen, Y. Li, J.W. Schwank, A review on Oxygen Storage Capacity of CeO2-Based materials: influence factors, measurement techniques, and applications in reactions related to Catalytic Automotive Emissions Control. Catal. Today. **327**, 90–115 (2019). https://doi.org/10.1016/j.cattod.2018.05.059
95. R.K. Singha, A. Shukla, A. Yadav, L.N.S. Konathala, R. Bal, Effect of Metal-Support Interaction on Activity and Stability of Ni-CeO2 Catalyst for partial oxidation of methane. Appl. Catal. B **202**, 473–488 (2017). https://doi.org/10.1016/j.apcatb.2016.09.060
96. J.C. Matsubu, S. Zhang, L. DeRita, N.S. Marinkovic, J.G. Chen, G.W. Graham, X. Pan, P. Christopher, Adsorbate-mediated strong metal–support interactions in oxide-supported rh catalysts. Nat. Chem. **9**, 120–127 (2017). https://doi.org/10.1038/nchem.2607
97. D. Titus, E.J.J. Samuel, S.M. Roopan, Nanoparticle characterization techniques. *Green Synthesis, Characterization and Applications of Nanoparticles* (Elsevier, Amsterdam, 2019), pp. 303–319
98. C.J. Chirayil, J. Abraham, R.K. Mishra, S.C. George, S. Thomas, Instrumental techniques for the characterization of nanoparticles. *Thermal and Rheological Measurement Techniques for Nanomaterials Characterization* (Elsevier, Amsterdam, 2017), pp. 1–36
99. K. Ye, K. Li, Y. Lu, Z. Guo, N. Ni, H. Liu, Y. Huang, H. Ji, P. Wang, An overview of Advanced methods for the characterization of Oxygen vacancies in materials. TRAC Trends Anal. Chem. **116**, 102–108 (2019). https://doi.org/10.1016/j.trac.2019.05.002
100. R. Murugan, G. Vijayaprasath, T. Mahalingam, G. Ravi, Enhancement of Room Temperature Ferromagnetic Behavior of Rf Sputtered Ni-CeO2 Thin films. Appl. Surf. Sci. **390**, 583–590 (2016). https://doi.org/10.1016/j.apsusc.2016.08.166
101. X. Du, D. Zhang, L. Shi, R. Gao, J. Zhang, Morphology Dependence of Catalytic Properties of Ni/CeO $_2$ nanostructures for Carbon Dioxide Reforming of methane. J. Phys. Chem. C **116**, 10009–10016 (2012). https://doi.org/10.1021/jp300543r
102. H. Ding, J. Yang, S. Ma, N. Yigit, J. Xu, G. Rupprechter, J. Wang, Large dimensional CeO 2 nanoflakes by microwave-assisted synthesis: lamellar nano-channels and surface oxygen vacancies promote catalytic activity. ChemCatChem **10**, 4100–4108 (2018). https://doi.org/10.1002/cctc.201800784
103. Z. Bian, Y.M. Chan, Y. Yu, S. Kawi, Morphology Dependence of Catalytic Properties of Ni/CeO2 for CO2 methanation: a kinetic and mechanism study. Catal. Today. **347**, 31–38 (2020). https://doi.org/10.1016/j.cattod.2018.04.067
104. L.C. Loc, P.H. Phuong, D. Putthea, N. Tri, N.T.T. Van, H.T. Cuong, Effect of CeO2 morphology on performance of NiO/CeO2 Catalyst in Combined Steam and CO2 reforming of CH4. Int. J. Nanotechnol. **15**, 968 (2018). https://doi.org/10.1504/IJNT.2018.099935
105. L. Atzori, M.G. Cutrufello, D. Meloni, C. Cannas, D. Gazzoli, R. Monaci, M.F. Sini, E. Rombi, Highly active NiO-CeO2 catalysts for synthetic Natural Gas production by CO2 methanation. Catal. Today. **299**, 183–192 (2018). https://doi.org/10.1016/j.cattod.2017.05.065
106. L.C. Loc, P.H. Phuong, N. Tri, Role of CeO2 promoter in NiO/α-Al2O3 catalyst for dry reforming of methane. AIP Conf. Proc. **1878**, 20033 (2017)
107. L. Bian, W. Wang, R. Xia, Z. Li, Ni-Based Catalyst Derived from Ni/Al Hydrotalcite-like compounds by the Urea Hydrolysis Method for CO Methanation. RSC Adv. **6**, 677–686 (2016). https://doi.org/10.1039/C5RA19748A
108. T. Mokrane, A.-G. Boudjahem, M. Bettahar, Benzene Hydrogenation over Alumina-supported Nickel nanoparticles prepared by Polyol Method. RSC Adv. **6**, 59858–59864 (2016). https://doi.org/10.1039/C6RA08527J
109. M. Chettibi, A.-G. Boudjahem, M. Bettahar, Synthesis of Ni/SiO2 nanoparticles for Catalytic Benzene Hydrogenation. Transition Met. Chem. **36**, 163–169 (2011). https://doi.org/10.1007/s11243-010-9449-8
110. S. VELU, S. GANGWAL, Synthesis of Alumina supported Nickel nanoparticle catalysts and evaluation of Nickel Metal dispersions by temperature programmed Desorption. Solid State Ion. **177**, 803–811 (2006). https://doi.org/10.1016/j.ssi.2006.01.031
111. R. WOJCIESZAK, Nickel Containing, MCM-41 and AlMCM-41 Mesoporous Molecular SievesCharacteristics and Activity in the hydrogenation of Benzene. Appl. Catal. Gen. **268**, 241–253 (2004). https://doi.org/10.1016/j.apcata.2004.03.047
112. G. Pacchioni, Oxygen vacancy: the invisible agent on oxide surfaces. ChemPhysChem **4**, 1041–1047 (2003). https://doi.org/10.1002/cphc.200300835
113. A.T. Bell, The impact of nanoscience on heterogeneous catalysis. Sci. (1979). **299**, 1688–1691 (2003). https://doi.org/10.1126/science.1083671
114. L. Zeng, Z. Cheng, J.A. Fan, L.-S. Fan, J. Gong, Metal Oxide Redox Chemistry for Chemical looping processes.

Nat. Rev. Chem. **2**, 349–364 (2018). https://doi.org/10.1038/s41570-018-0046-2
115. J. Su, X. Zou, J.-S. Chen, Self-modification of Titanium Dioxide materials by Ti 3 + and/or Oxygen vacancies: new insights into defect Chemistry of Metal Oxides. RSC Adv. **4**, 13979–13988 (2014). https://doi.org/10.1039/C3RA47757F
116. A.R. Puigdollers, P. Schlexer, S. Tosoni, G. Pacchioni, Increasing Oxide Reducibility: the role of Metal/Oxide interfaces in the formation of Oxygen vacancies. ACS Catal. **7**, 6493–6513 (2017). https://doi.org/10.1021/acscatal.7b01913
117. G. Zhao, F. Yang, Z. Chen, Q. Liu, Y. Ji, Y. Zhang, Z. Niu, J. Mao, X. Bao, P. Hu et al., Metal/Oxide Interfacial effects on the selective oxidation of primary alcohols. Nat. Commun. **8**, 14039 (2017). https://doi.org/10.1038/ncomms14039
118. Z. Liu, S.D. Senanayake, J.A. Rodriguez, Elucidating the Interaction between Ni and CeOx in ethanol steam reforming catalysts: a perspective of recent studies over Model and Powder systems. Appl. Catal. B **197**, 184–197 (2016). https://doi.org/10.1016/j.apcatb.2016.03.013
119. A. Beste, S.H. Overbury, Pathways for ethanol dehydrogenation and dehydration catalyzed by Ceria (111) and (100) surfaces. J. Phys. Chem. C **119**, 2447–2455 (2015). https://doi.org/10.1021/jp509686f
120. K. Mudiyanselage, I. Al-Shankiti, A. Foulis, J. Llorca, H. Idriss, Reactions of ethanol over CeO2 and Ru/CeO2 catalysts. Appl. Catal. B **197**, 198–205 (2016). https://doi.org/10.1016/j.apcatb.2016.03.065
121. Y. Choi, M. Scott, T. Söhnel, H. Idriss, A DFT + U computational study on Stoichiometric and Oxygen Deficient M–CeO 2 systems (M = pd 1, rh 1, Rh 10, pd 10 and rh 4 pd 6). Phys. Chem. Chem. Phys. **16**, 22588–22599 (2014). https://doi.org/10.1039/C4CP03366C
122. G. Słowik, M. Greluk, M. Rotko, A. Machocki, Influence of composition and morphology of the active phase on the Catalytic properties of Cobalt-Nickel catalysts in the Steam reforming of ethanol. Mater. Chem. Phys. **258**, 123970 (2021). https://doi.org/10.1016/j.matchemphys.2020.123970
123. M.-R. Li, G.-C. Wang, The mechanism of ethanol steam reforming on the Co0 and Co2 + sites: a DFT study. J. Catal. **365**, 391–404 (2018). https://doi.org/10.1016/j.jcat.2018.07.002
124. Z. Hao, L. Guo, M. Xing, Q. Zhang, Mechanistic study of ethanol steam reforming on TM–Mo 6 S 8 clusters: a DFT study. Catal. Sci. Technol. **9**, 1631–1643 (2019). https://doi.org/10.1039/C8CY02151A
125. K.D. Punase, N. Rao, P.A. Vijay, Review on mechanistic kinetic models of ethanol steam reforming for Hydrogen Production using a fixed Bed Reactor. Chem. Pap. **73**, 1027–1042 (2019). https://doi.org/10.1007/s11696-018-00678-6
126. S. Ogo, Y. Sekine, Recent progress in ethanol steam reforming using non-noble transition metal catalysts: a review. Fuel Process. Technol. **199**, 106238 (2020). https://doi.org/10.1016/j.fuproc.2019.106238
127. Q. Zhang, L. Guo, X. Zheng, M. Xing, Z. Hao, Insight into the reaction mechanism of ethanol steam reforming Catalysed by Co–Mo $_6$ S $_8$. Mol. Phys. **117**, 416–430 (2019). https://doi.org/10.1080/00268976.2018.1521011
128. de S.M. Lima, da A.M. Silva, da L.O.O. Costa, U.M. Graham, G. Jacobs, B.H. Davis, L.V. Mattos, F.B. Noronha, Study of Catalyst deactivation and reaction mechanism of Steam Reforming, partial oxidation, and Oxidative Steam Reforming of Ethanol over Co/CeO2 Catalyst. J. Catal. **268**, 268–281 (2009). https://doi.org/10.1016/j.jcat.2009.09.025
129. S. Lin, J. Huang, X. Gao, X. Ye, H. Guo, Theoretical insight into the Reaction Mechanism of Ethanol Steam Reforming on Co(0001). J. Phys. Chem. C **119**, 2680–2691 (2015). https://doi.org/10.1021/jp512000k
130. S. Wang, W. Guo, L. Guo, X. Li, Q. Wang, Experimental and subsequent mechanism research on the Steam reforming of ethanol over a Ni/CeO $_2$ Catalyst. Int. J. Green. Energy. **12**, 694–701 (2015). https://doi.org/10.1080/15435075.2013.834821
131. Z. Hao, L. Guo, Y. Han, Insight into the mechanism of ethanol steam reforming on TM/Mo6S8 clusters catalysts: a theoretical investigation. Int. J. Hydrogen Energy. **44**, 23947–23958 (2019). https://doi.org/10.1016/j.ijhydene.2019.07.102
132. J.E. Sutton, P. Panagiotopoulou, X.E. Verykios, D.G. Vlachos, D.F.T. Combined, Microkinetic, and experimental study of ethanol steam reforming on pt. J. Phys. Chem. C **117**, 4691–4706 (2013). https://doi.org/10.1021/jp312593u
133. A.T.F. Afolabi, C.-Z. Li, P.N. Kechagiopoulos, Microkinetic Modelling and Reaction Pathway Analysis of the Steam Reforming of Ethanol over Ni/SiO2. Int. J. Hydrogen Energy. **44**, 22816–22830 (2019). https://doi.org/10.1016/j.ijhydene.2019.07.040
134. Z. Liu, T. Duchoň, H. Wang, E.W. Peterson, Y. Zhou, S. Luo, J. Zhou, V. Matolín, D.J. Stacchiola, J.A. Rodriguez et al., Mechanistic insights of ethanol steam reforming over Ni–CeO x (111): the importance of Hydroxyl groups for suppressing Coke formation. J. Phys. Chem. C **119**, 18248–18256 (2015). https://doi.org/10.1021/acs.jpcc.5b04310

Publisher's Note Springer Nature remains neutral with regard to jurisdictional claims in published maps and institutional affiliations.

Springer Nature or its licensor (e.g. a society or other partner) holds exclusive rights to this article under a publishing agreement with the author(s) or other rightsholder(s); author self-archiving of the accepted manuscript version of this article is solely governed by the terms of such publishing agreement and applicable law.